

## Systematic Phase Curve Study of Known Transiting Systems from Year 1 of the *TESS* Mission

IAN WONG,<sup>1,\*</sup> AVI SHPORER,<sup>2</sup> TANSU DAYLAN,<sup>2,†</sup> BJÖRN BENNEKE,<sup>3</sup> TARA FETHEROLF,<sup>4</sup> STEPHEN R. KANE,<sup>5</sup>  
GEORGE R. RICKER,<sup>2</sup> ROLAND VANDERSPEK,<sup>2</sup> DAVID W. LATHAM,<sup>6</sup> JOSHUA N. WINN,<sup>7</sup> JON M. JENKINS,<sup>8</sup>  
PATRICIA T. BOYD,<sup>9</sup> ANA GLIDDEN,<sup>1,2</sup> ROBERT F. GOEKE,<sup>2</sup> LIZHOU SHA,<sup>2</sup> ERIC B. TING,<sup>8</sup> AND DANIEL YAHALOMI<sup>6</sup>

<sup>1</sup>*Department of Earth, Atmospheric and Planetary Sciences, Massachusetts Institute of Technology, Cambridge, MA 02139, USA*

<sup>2</sup>*Department of Physics and Kavli Institute for Astrophysics and Space Research, Massachusetts Institute of Technology, Cambridge, MA 02139, USA*

<sup>3</sup>*Department of Physics and Institute for Research on Exoplanets, Université de Montréal, Montréal, QC, Canada*

<sup>4</sup>*Department of Physics and Astronomy, University of California, Riverside, CA 92521, USA*

<sup>5</sup>*Department of Earth and Planetary Sciences, University of California, Riverside, CA 92521, USA*

<sup>6</sup>*Center for Astrophysics | Harvard & Smithsonian, 60 Garden Street, Cambridge, MA 02138, USA*

<sup>7</sup>*Department of Astrophysical Sciences, Princeton University, Princeton, NJ 08544, USA*

<sup>8</sup>*NASA Ames Research Center, Moffett Field, CA 94035, USA*

<sup>9</sup>*Astrophysics Science Division, NASA Goddard Space Flight Center, Greenbelt, MD 20771, USA*

### ABSTRACT

We present a systematic phase curve analysis of known transiting systems observed by the *Transiting Exoplanet Survey Satellite* during Year 1 of the Primary Mission. Using theoretical predictions for the amplitude of the planetary longitudinal atmospheric brightness modulation, stellar ellipsoidal distortion and Doppler boosting, as well as brightness considerations to select targets with likely detectable signals, we applied a uniform data processing and light curve modeling framework to fit the full-orbit phase curves of 19 transiting systems with planet-mass or brown dwarf companions. Statistically significant secondary eclipse depths and/or atmospheric brightness modulation amplitudes were measured for HIP 65A, WASP-72, WASP-100, WASP-111, and WASP-122/KELT-14. For WASP-100b, we found marginal evidence that the brightest region of the atmosphere is shifted eastward by  $14^{\circ}2 \pm 4^{\circ}6$  away from the substellar point. We found significant ellipsoidal distortion signals in the light curves of HIP 65A, TOI-503, and WASP-30, with TOI-503 also exhibiting Doppler boosting. The measured amplitudes of these signals agree with the predictions of theoretical models. From our light curve fits, we also measured updated and refined orbital ephemerides and transit shape parameters. Combining the optical secondary eclipse depths with previously published *Spitzer* 3.6 and 4.5  $\mu\text{m}$  measurements, we derived dayside brightness temperatures and visible-light geometric albedos for a subset of the analyzed systems. We find a tentative correlation between increasing dayside temperature and increasing geometric albedo in the *TESS* bandpass, suggesting enhanced atmospheric reflectivity and/or additional opacity sources contributing to the visible-light flux for planets with  $T_{\text{day}} > 2200$  K.

**Keywords:** binaries: eclipsing — planetary systems — techniques: photometric

### 1. INTRODUCTION

Since the start of science observations on 2018 July 25, the *Transiting Exoplanet Survey Satellite* (*TESS*) has been observing most of the sky in search of new transiting exoplanets around bright, nearby stars. In addition to the thousands of planet candidates and several dozen confirmed planets that the mission has de-

tected to date, hundreds of previously discovered exoplanet systems have been observed, providing nearly continuous broadband visible photometry spanning at least one month for every target. This treasury of light curves has proven to be an invaluable resource for time-domain astronomy of known exoplanet systems.

*TESS* has been especially fruitful for the study of orbital phase curves. Long-baseline photometric monitoring of transiting systems can reveal the secondary eclipse, when the orbiting companion is occulted by the host star, as well as photometric variations phased to the orbital period. Short-period systems are expected to be tidally locked (e.g., [Mazeh 2008](#)), with fixed day-side and night-side hemispheres that may differ greatly

Corresponding author: Ian Wong  
iwong@mit.edu

\* 51 Pegasi b Fellow

† Kavli Fellow

in temperature. The changing viewing phase of the orbiting companion results in a periodic modulation of the observed atmospheric brightness with maxima and minima near mid-eclipse (superior conjunction) and mid-transit (inferior conjunction), respectively (see [Parmen-tier & Crossfield 2017](#), for a review of this phase curve component).

The depth of the secondary eclipse corresponds to the relative brightness of the companion’s dayside hemisphere. At visible wavelengths, the eclipse depth contains contributions from both thermal emission and reflected starlight. The addition of secondary eclipse measurements at infrared wavelengths breaks the degeneracy between reflected light and thermal emission, yielding direct constraints on the optical geometric albedo, an important quantity for inferring the presence of clouds and hazes on the dayside hemisphere. When combined with measurements of the amplitude of the atmospheric brightness modulation, one can deduce the dayside and nightside temperatures. Meanwhile, a detected phase shift in the atmospheric brightness modulation indicates an offset in the region of maximum brightness relative to the substellar point, which may be caused by inhomogeneous clouds (e.g., [Shporer & Hu 2015](#)) or an eastward-shifted dayside hotspot due to superrotating equatorial winds (e.g., [Perna et al. 2012](#); [Perez-Becker & Showman 2013](#)).

For massive orbiting companions, gravitational interactions can cause variations in the host star’s brightness that are detectable in precise visible-light phase curves. First, the Doppler boosting signal is produced when the radial velocity (RV) modulation of the star induced by the gravitational pull of the orbiting companion leads to periodic blue- and red-shifting of the stellar spectrum as well as modulations in photon emission rate in the observer’s direction (e.g., [Shakura & Postnov 1987](#); [Loeb & Gaudi 2003](#); [Zucker et al. 2007](#)). Second, the companion’s gravity raises tidal bulges on the star, with the long dimension aligned with the star-companion axis (e.g., [Morris 1985](#); [Morris & Naftilan 1993](#); [Pfahl et al. 2008](#)). This produces a modulation in the star’s sky-projected area and apparent flux that comes to maximum at the quadratures, resulting in a phase curve signal with a leading term at the first harmonic of the orbital phase. A detailed overview of the astrophysics of visible light phase curves is provided in [Shporer \(2017\)](#).

Analyses of individual high signal-to-noise phase curves from the *TESS* mission have been published for several systems, including WASP-18 ([Shporer et al. 2019](#)), WASP-19 ([Wong et al. 2020b](#)), WASP-100 ([Jansen & Kipping 2020](#)), WASP-121 ([Bourrier et al. 2019](#); [Daylan et al. 2019](#)), and KELT-9 ([Wong et al. 2020d](#)). These studies have reported robust detections of phase curve signals attributed to all of the aforementioned processes. Building upon these previous studies, as well as the legacy of analogous works from the *Kepler* era (e.g., [Esteves et al. 2013, 2015](#); [Angerhausen et al.](#)

[2015](#)), we seek to expand the search for phase curve signals in *TESS* photometry to cover all confirmed star-planet systems. By extending our analysis to systems with lower signal-to-noise datasets, we will maximize the science yield of the *TESS* mission in the realm of phase curves.

In this paper, we present a systematic phase curve study of known transiting systems observed during the first year of the *TESS* mission. We consider both planetary-mass companions and brown dwarfs, and include targets that were discovered prior to the *TESS* mission as well as new confirmed systems discovered by *TESS*. Special attention is given to utilizing a uniform data processing and phase curve modeling framework and applying a consistent treatment of instrumental systematics across all datasets, analogous to the techniques used in our previously published studies.

The paper is organized as follows. Section 2 describes the *TESS* observations and data processing techniques used to produce the light curves for our fits. The target selection criteria for filtering out systems with phase curve signals that are likely to be undetectable are detailed in Section 3. The results of the phase curve analyses are presented in Section 4. In Section 5, we discuss these results in the context of theoretical predictions of the gravitational phase curve amplitudes; we also combine previously published *Spitzer* secondary eclipse measurements with our *TESS*-band eclipse depths to calculate the dayside brightness temperatures and optical geometric albedos for a subset of the analyzed systems. We summarize the main results of this work in Section 6.

## 2. LIGHT CURVES AND DATA ANALYSIS

### 2.1. *TESS* observations

During Year 1 of the *TESS* Primary Mission (2018 July 25 to 2019 July 18), the spacecraft observed most of the southern ecliptic hemisphere. *TESS* has four identical wide-field cameras, each with an effective aperture diameter of 10 cm. The combined field of view of  $24^\circ \times 96^\circ$  is oriented with the long axis along a line of constant ecliptic longitude. In latitude, the field of view begins at  $-6^\circ$  and reaches  $12^\circ$  past the southern ecliptic pole. The Southern Sky was divided into 13 Sectors; each Sector was observed for 27.4 days, corresponding to two geocentric spacecraft orbits, with an interruption in data collection between orbits during perigee for data downlink.

Each of the four cameras consists of four CCDs with a total on-sky area of  $4096 \times 4096$  pixels. *TESS* utilizes a red-optical bandpass spanning 600–1000 nm, centered on the Cousins I-band ( $\lambda = 786.5$  nm). The entire array is read out at 2 second intervals, with individual frames combined on board into  $11 \times 11$  pixel stamps at 2 minute cadence and full-frame images at 30 minute cadence prior to downlink. The targets for which 2-minute data are compiled have been selected from the *TESS* Input Catalog (TIC; [Stassun et al. 2018](#)) and include al-

most all of the bright, known transiting exoplanet systems within the *TESS* Sectors.

The downlinked pixel stamps are passed through the Science Processing Operations Center (SPOC) pipeline (Jenkins et al. 2016). After the optimal photometric extraction apertures are determined, two types of light curves are produced: Simple Aperture Photometry (SAP) and Presearch Data Conditioning (PDC) light curves. To construct the PDC light curves, the raw aperture photometry is detrended for common-mode instrumental systematics using cotrending basis vectors empirically calculated from other sources on the corresponding detector (Smith et al. 2012; Stumpe et al. 2014). The PDC light curves are also corrected for flux contamination from nearby stars. Both the SAP and PDC light curves are publicly released and hosted on the Mikulski Archive for Space Telescopes (MAST). For all the systems studied in this paper, we found the PDC light curves to be cleaner than the SAP light curves, showing significantly fewer short-timescale flux variations and reduced scatter. Analyses of the same target using PDC and SAP light curves yielded statistically consistent parameter values in all cases.

Momentum dumps are scheduled 2–4 times per spacecraft orbit in order to reset the onboard reaction wheels. These events often lead to discontinuities in the flux time series, as well as occasional flux ramps before or after lasting up to 1 day. To adequately model the residual instrumental systematics in our light curve fits, we followed previous work (Wong et al. 2020b,d) and split each orbit’s time series into discrete segments, separated by the momentum dumps. Each of these segments is assigned its own systematics model in the joint fits (see Sections 2.2 and 2.3 for details).

In cases where discernible flux ramps are present, we chose to trim these short-timescale features from the time series, because retaining them would necessitate significantly higher-order systematics detrending functions and may lead to biases in the fitted astrophysical phase curve amplitudes. All of the trimmed time intervals were set to multiples of 0.25 days.

Periods of abnormal spacecraft operation and significant scattered light on the detector are automatically flagged by the SPOC pipeline, and we removed all flagged points from the time series. Prior to fitting, we applied a 16-point wide moving median filter to the light curve (excluding regions near primary transits) and trimmed  $>3\sigma$  outliers. The flagged point and outlier trimming process typically removed less than 5% of the data points.

A full list of the data segments considered in this work is provided in the Appendix. We did not include any data segment that spans less than 1 day (much shorter than the orbital period of most of our targets). In a handful of cases, severe systematic artifacts (e.g., sharp, short-term flux variations and periods of significantly increased scatter) were present in individual segments;

because such features are not readily removed using typical systematics detrending methods, we discarded these segments in their entirety prior to fitting.

## 2.2. Full phase curve model

The light curve modeling in this work is identical to the methods used in previous papers (Shporer et al. 2019; Wong et al. 2020b,d). The core computational framework for our analysis is the ExoTEP pipeline (e.g., Benneke et al. 2019; Wong et al. 2020a) — a modular, Python-based tool for data extraction and light curve fitting.

The transit and secondary eclipse light curves —  $\lambda_t(t)$  and  $\lambda_e(t)$ , respectively — are modeled using *batman* (Kreidberg 2015). The out-of-eclipse phase curve variation is appropriately divided into terms describing variations in the orbiting companion’s flux  $\psi_p(t)$  and those attributed to the host star’s flux  $\psi_*(t)$ . Defining the orbital phase as  $\phi \equiv 2\pi(t - T_0)/P$ , where  $T_0$  is the mid-transit time, and  $P$  is the orbital period, the component photometric signals are expressed as

$$\psi_p(t) = \bar{f}_p - A_{\text{atm}} \cos(\phi + \delta), \quad (1)$$

$$\psi_*(t) = 1 - A_{\text{ellip}} \cos(2\phi) + A_{\text{Dopp}} \sin(\phi). \quad (2)$$

Here,  $\bar{f}_p$  is the average relative brightness of the orbiting companion, and  $A_{\text{atm}}$  and  $\delta$  are the semiamplitude and phase shift of the object’s atmospheric brightness modulation. The parameter  $\delta$  is defined such that a positive value denotes an eastward shift in the region of maximum brightness.  $A_{\text{ellip}}$  and  $A_{\text{Dopp}}$  are the semiamplitudes of the ellipsoidal distortion and Doppler beaming phase curve modulations. The sign convention in Equations (1) and (2) is chosen so as to yield positive amplitudes, assuming the expected behavior for the associated physical processes (e.g., Shporer 2017). In the case where both  $\bar{f}_p$  and  $A_{\text{atm}}$  are robustly detected, the secondary eclipse depth and nightside flux are, by definition,  $D_d = \bar{f}_p - A_{\text{atm}} \cos(\pi + \delta)$  and  $D_n = \bar{f}_p - A_{\text{atm}} \cos(\delta)$ , respectively.

The astrophysical phase curve model, renormalized such that the combined average star+companion brightness is unity, is given by

$$\psi(t) = \frac{\psi_*(t)\lambda_t(t) + \lambda_e(t)\psi_p(t)}{1 + \bar{f}_p}. \quad (3)$$

All remaining temporal variations in the PDC light curve segments (e.g., from residual uncorrected instrumental systematics or stellar variability) are described by generalized polynomial functions in time,

$$S_N^{\{i\}}(t) = \sum_{j=0}^N c_j^{\{i\}}(t - t_0)^j, \quad (4)$$

where  $t_0$  is the time of the first data point in segment  $i$ , and  $N$  is the order of the detrending polynomial. The

full phase curve and systematics model is

$$f(t) = S_N^{\{i\}}(t)|_{i=1-6} \times \psi(t). \quad (5)$$

The optimal polynomial order for each segment was determined by carrying out full phase curve fits to the individual segment light curves. When selecting the orders, we considered both the Bayesian Information Criterion  $\text{BIC} \equiv \gamma \log m - 2 \log L$  and the Akaike Information Criterion  $\text{AIC} \equiv 2\gamma - 2 \log L$ , where  $\gamma$  is the number of free parameters in the fit,  $m$  is the number of data points in the segment, and  $L$  is the maximum log-likelihood. For the majority of data segments, minimization of the BIC and AIC yielded the same optimal polynomial order; for cases in which the AIC preferred a higher order than the BIC, we conservatively chose the order that minimized the BIC in order to reduce the number of free systematics parameters in the fit. Using the higher orders did not incur any significant changes to the astrophysical parameter values from the overall joint fits.

### 2.3. Model fitting

In the joint fits, we allowed the transit depth (parameterized by the planet-star radius ratio  $R_p/R_*$ ), orbital ephemeris (mid-transit time  $T_0$  and orbital period  $P$ ), and transit shape parameters (impact parameter  $b$  and scaled orbital semi-major axis  $a/R_*$ ) to vary freely. In most cases, the constraints we derived for  $b$  and  $a/R_*$  are comparable to or more precise than available literature values, and as such, we did not choose to place priors on these parameters in the fits. For all of the systems analyzed in this paper, the available data are consistent with a circular orbit. We assumed the orbital eccentricity  $e$  is equal to zero during our fitting procedure.

To achieve conservative constraints on the transit depth and other system parameters, given the uncertainties in theoretical limb darkening models, we typically used a quadratic limb darkening model and allowed both coefficients —  $u_1$  and  $u_2$  — to vary freely. An exception to this rule was HIP 65A, which has a grazing transit ( $b > 1$ ): because the stellar limb darkening profile is not well-constrained in such instances, we chose to fix the limb darkening coefficients to the values listed in [Claret \(2018\)](#) for the nearest available combination of stellar parameters.

For each target, we ran a suite of joint fits with various subsets of the phase curve parameters  $\bar{f}_p$ ,  $A_{\text{atm}}$ ,  $\delta$ ,  $A_{\text{ellip}}$ , and  $A_{\text{Dopp}}$ . When selecting the final set of results to present in this paper, we considered both the BIC and AIC, generally choosing the fit that minimizes the BIC. By incurring a penalty for each additional free parameter included in the phase curve model, scaled by the length of the time series, this process robustly determines which phase curve components show statistically significant signals in the data.

In addition to the systematics model coefficients  $\{c_j^{\{i\}}\}$ , we fit for a uniform per-point uncertainty  $\sigma_i$

for each segment in order to ensure that the resultant reduced  $\chi^2$  value is unity and to obtain realistic uncertainties on the astrophysical parameters.

ExoTEP utilizes the affine-invariant Markov Chain Monte Carlo routine `emcee` ([Foreman-Mackey et al. 2013](#)) to simultaneously compute the posterior distributions of all free parameters. In each fit, we set the number of walkers to four times the number of free parameters and initiated each chain near the best-fit parameter values from the corresponding individual segment fits. We typically set the chain lengths to 15,000–25,000 steps and discarded a burn-in equal to 60% of each chain prior to calculating the posterior distributions. As a test for convergence, we checked that the Gelman-Rubin statistic  $\hat{R}$  is below 1.1 ([Gelman & Rubin 1992](#)).

### 3. TARGET SELECTION

The input database for our target selection included all known transiting planetary systems as well as new confirmed *TESS* discoveries, published or submitted as of 2019 December 1. We also searched through the catalog of known transiting brown dwarf systems, as compiled in [Carmichael et al. \(2019\)](#) and [Mireles et al. \(2020\)](#). To select targets with potentially detectable phase curve signals and secondary eclipses, we considered both photometric precision and theoretical predicted values for the various signals. Extrapolating from the experience of our previous *TESS* phase curve studies ([Shporer et al. 2019](#); [Wong et al. 2020b,d](#)), we limited our focus to systems with apparent *TESS*-band magnitudes brighter than 12.5 mag; this benchmark corresponds to a scaled 1-hour combined differential photometric precision of roughly 1000 ppm ([Sullivan et al. 2015](#); [Stassun et al. 2017](#)). We also only considered systems for which 2-minute cadence data from the SPOC pipeline are available, in order to adequately resolve the ingress and egress of individual transits and secondary eclipses.

Systems displaying significant stellar variability other than the phased photometric modulations studied here (originating from, for example, pulsations or starspots) are challenging for phase curve analyses. The problems are particularly severe when the characteristic timescale of the variability is shorter than the orbital period, because techniques for detrending such additional photometric modulation can strongly bias the resultant measured astrophysical phase curve signals, or even remove it altogether. In this work, we did not analyze systems that show discernible short-term photometric variability on timescales shorter than or comparable to the orbital period. Several otherwise promising systems were rejected due to this variability constraint, including WASP-87A, WASP-167, and K2-237.

For transiting planetary-mass companions, the phase curve feature with the largest relative amplitude is typically the secondary eclipse. We calculated the predicted secondary eclipse depth using basic flux balance consid-

erations, with the inclusion of reflected starlight (e.g., Esteves et al. 2013, 2015; Shporer 2017):

$$D'_d = \left(\frac{R_p}{R_*}\right)^2 \frac{\int B_\lambda(T_p)\tau(\lambda) d\lambda}{\int B_\lambda(T_*)\tau(\lambda) d\lambda} + A_g \left(\frac{R_p}{a}\right)^2. \quad (6)$$

Here, for simplicity, we have approximated the star and planet flux as blackbodies  $B_\lambda$  with temperatures  $T_p$  and  $T_*$ , respectively. The fluxes are integrated over the *TESS* bandpass, with the associated transmission function  $\tau(\lambda)$ . The contribution of reflected light to the eclipse depth is parameterized by the geometric albedo in the *TESS* band:  $A_g$ .

To compute the maximum limiting case for the planet’s dayside temperature, we stipulated zero heat distribution across the planet’s surface (i.e., instant reradiation). We assumed Lambertian scattering when relating Bond albedo to geometric albedo:  $A_B \equiv \frac{3}{2}A_g$ . It follows that the planet’s dayside temperature can be expressed as (e.g., Esteves et al. 2013, 2015)

$$T_p = T_* \sqrt{\frac{R_*}{a}} \left[ \frac{2}{3} \left( 1 - \frac{3}{2}A_g \right) \right]^{1/4}. \quad (7)$$

The orbiting companions with potentially detectable secondary eclipses at visible wavelengths are almost all hot Jupiters and brown dwarfs. Both published geometric albedo measurements (e.g., Heng & Demory 2013; Esteves et al. 2015) and atmospheric models (e.g., Mayorga et al. 2019) indicate very low typical reflectivities for these objects, particularly in the red-optical.

We selected systems with  $D'_d > 100$  ppm, assuming  $A_g = 0.1$  in the *TESS* band. The list of known transiting systems in the ecliptic Southern Sky without previously published phase curves that satisfy the aforementioned constraints on brightness, stellar variability, and predicted secondary eclipse depth is as follows: HATS-24 (Bento et al. 2017), WASP-4 (Wilson et al. 2008), WASP-5 (Anderson et al. 2008), WASP-36 (Smith et al. 2012), WASP-43 (Hellier et al. 2011), WASP-46 (Anderson et al. 2012), WASP-64 (Gillon et al. 2013), WASP-72 (Gillon et al. 2013), WASP-77A (Maxted et al. 2013), WASP-78 (Smalley et al. 2012), WASP-82 (West et al. 2016), WASP-111 (Anderson et al. 2014), WASP-122/KELT-14 (Turner et al. 2016; Rodriguez et al. 2016), WASP-142 (Hellier et al. 2017), and WASP-173A (Hellier et al. 2019). We also include WASP-100 (Hellier et al. 2014), the phase curve of which has been published by Jansen & Kipping (2020); in this paper, we present our independent analysis of the *TESS* light curve.

For the most massive short-period planets and brown dwarfs, the gravitationally induced phase curve signals — ellipsoidal distortion and Doppler boosting — may be detectable with *TESS*, as was the case with WASP-18 (Shporer et al. 2019) and KELT-9 (Wong et al. 2020d). The leading term of the ellipsoidal distortion signal has

a semiamplitude of (e.g., Morris 1985; Shporer 2017)

$$A'_{\text{ellip}} = \alpha_{\text{ellip}} \frac{M_p}{M_*} \left(\frac{R_*}{a}\right)^3 \sin^2 i, \quad (8)$$

where  $M_p$  and  $M_*$  are the planet and stellar masses, respectively,  $i$  is the orbital inclination, and the prefactor  $\alpha_{\text{ellip}}$  is related to the linear limb-darkening and gravity-darkening coefficients  $u$  and  $g$  for the host star as follows:

$$\alpha_{\text{ellip}} = \frac{3}{20} \frac{(u+15)(g+1)}{3-u}. \quad (9)$$

Tabulated values of  $u$  and  $g$  calculated for the *TESS* bandpass can be found in Claret (2017).

The Doppler boosting semiamplitude is related to the system’s radial velocity (RV) semiamplitude  $K_{\text{RV}}$  by (e.g., Loeb & Gaudi 2003; Shporer 2017)

$$A'_{\text{Dopp}} = \alpha_{\text{Dopp}} \frac{K_{\text{RV}}}{c}, \quad (10)$$

where  $c$  is the speed of light and the beaming factor  $\alpha_{\text{Dopp}}$  is of order unity and depends on the logarithmic derivative of the host star’s flux with respect to wavelength, integrated over the *TESS* bandpass:

$$\alpha_{\text{Dopp}} = 3 - \left\langle \frac{d \log F_\nu}{d \log \nu} \right\rangle_{\text{TESS}}. \quad (11)$$

Using published system parameters for targets that satisfy the aforementioned brightness and variability constraints, we calculated predicted values for  $A'_{\text{ellip}}$  and  $A'_{\text{Dopp}}$  and selected systems for which one or both of these amplitudes exceed 25 ppm. From this, we obtained three additional systems to include in our analysis — HIP 65A (Nielsen et al. 2020), WASP-30 (Anderson et al. 2011), and TOI-503 (Šubjak et al. 2019) — for a total of 19 targets.

## 4. RESULTS

For each of the 19 targets selected for detailed analysis, we fit the combined light curve (i.e., all utilized segments; see Appendix) to the full phase curve and systematics model in Equation (5). We ran a series of fits with different combinations of phase curve components, comparing the BIC of each run with the BIC of a fit with no phase curve components (secondary eclipse or sinusoidal terms), which we hereafter refer to as the null case. Systems for which the null case has the lowest BIC are considered nondetections or marginal detections; they are discussed briefly in Section 4.1. The seven targets for which statistically robust signals were measured are discussed individually in the subsequent subsections.

**Table 1.** Marginal Detections and Nondetections

Target	TOI	Sector	$T^a$	$D_{d,\text{pred}}^b$	$D_{d,\text{meas}}^b$
HATS-24	1084	13	12.2	280	$240^{+110}_{-80}$
WASP-4	232	2	11.8	230	$130^{+80}_{-70}$
WASP-5	250	2	11.5	100	$<140$ ( $2\sigma$ )
WASP-36	567	8	12.1	120	$120^{+100}_{-80}$
WASP-43	656	9	11.0	170	$170^{+80}_{-70}$
WASP-46	101	1	12.4	140	$120^{+120}_{-90}$
WASP-64	473	6,7	12.0	100	$230^{+120}_{-110}$
WASP-77A	398	4	9.5	130	$55^{+20}_{-18}$
WASP-78	449	5	11.8	160	$220^{+80}_{-90}$
WASP-82	453	5	9.5	130	$78^{+27}_{-28}$
WASP-142	578	8	12.3	150	$210^{+170}_{-120}$
WASP-173A	241	2	10.9	140	$140^{+60}_{-50}$

**Notes.**<sup>a</sup> Apparent magnitude in the *TESS* bandpass.<sup>b</sup> Predicted and measured secondary eclipse depths, in parts-per-million. Predictions assume  $A_g = 0.1$  and zero heat transport to the nightside.

#### 4.1. Marginal detections and nondetections

Out of the 19 targets analyzed in this paper, 12 showed no robust phase curve signals of any kind. For most of these systems, the highest signal-to-noise phase curve component is the secondary eclipse. These marginal detections and nondetections tended to occur in relatively faint systems, illustrating the important limiting role that photometric precision plays in phase curve detectability.

We list the marginal detections and nondetections in Table 1. The secondary eclipse depths (or upper limit) derived from the phase curve fit including both parameters that describe the planet’s atmospheric brightness modulation ( $\bar{f}_p$  and  $A_{\text{atm}}$ ) are given. We also include the corresponding predicted values, computed following the prescription described in Section 3. The measured secondary eclipse depths have formal statistical significances ranging from  $<1\sigma$  to  $\sim 3\sigma$ , with the fitted values broadly in agreement with the predictions. For all of these systems, the BIC of the null case was lower than the next-lowest case by a margin of at least  $\Delta\text{BIC} = 2.2$ . Even though these secondary eclipse detections fail the BIC test, we will utilize some of them to place rough constraints on the visible geometric albedo in Section 5.2.

#### 4.2. HIP 65A

The discovery of this system was reported in Nielsen et al. (2020). The system, observed by *TESS* during Sectors 1 and 2, consists of a  $3.23 M_{\text{Jup}}$  planet on a grazing 0.98-day orbit around an active  $0.79 M_{\odot}$  K-dwarf. Due to the small occulted area of the planet during superior conjunction, as well as the relatively low stellar temperature, the predicted depth of the secondary eclipse is very small, and indeed, we did not measure

any significant secondary eclipse in our fits. The full list of fitted astrophysical parameters from the lowest-BIC run is given in Table 2. Due to the extremely grazing nature of the transit, we placed Gaussian priors on the quadratic limb darkening coefficients. We extrapolated the tabulated coefficient values from Claret (2018) to the effective temperature and surface gravity measurements reported in Nielsen et al. (2020) ( $T_{\text{eff}} = 4590$  K,  $\log g = 4.611$ ) and set the width of the Gaussian to 0.05 for both coefficients:  $(u_1, u_2) = (0.50 \pm 0.05, 0.16 \pm 0.05)$ .

The phase-folded, systematics-removed light curve and best-fit phase curve model are shown in Figure 1. For this and all subsequent plots, the binning interval is chosen so that 75 bins span the orbital period. We detected statistically significant phase curve amplitudes corresponding to the atmospheric brightness modulation and ellipsoidal distortion:  $A_{\text{atm}} = 30.4^{+8.5}_{-7.7}$  ppm and  $A_{\text{ellip}} = 29.0^{+7.7}_{-7.9}$  ppm. We also measured a marginal Doppler boosting amplitude  $A_{\text{Dopp}} = 18.4 \pm 7.0$  ppm. However, including this term in the joint fit led to a large increase in the BIC and only a slight improvement in the AIC ( $\Delta\text{AIC} < 3$ ), and therefore, we do not include that amplitude in the results presented in Table 2.

Nielsen et al. (2020) carried out an independent fit for the phase curve components and obtained the following values:  $A_{\text{atm}} = 57.5 \pm 4.7$  ppm,  $A_{\text{ellip}} = 33.0 \pm 4.7$  ppm, and  $A_{\text{Dopp}} = 15.4 \pm 4.5$  ppm. We note that their approach involved applying a polynomial spline to the light curve prior to fitting to remove long-term trends (without accounting for the momentum dumps and the associated flux ramps) and then phase-folding and binning the light curve, as opposed to our approach of fitting these trends simultaneously with the astrophysical model to the unbinned and unfolded light curve. This is the primary reason for the smaller uncertainties on the phase curve amplitudes in their analysis. Furthermore, Nielsen et al. (2020) did not remove the two anomalous ramps in the vicinity of momentum dumps that we excised from the light curve prior to fitting (see Appendix). When including both gravitationally induced phase curve terms in the astrophysical model, the fitted values for  $A_{\text{ellip}}$  and  $A_{\text{Dopp}}$  from our two analyses agree to well within  $1\sigma$ . Meanwhile, the atmospheric brightness modulation amplitudes differ by  $2.8\sigma$ . All other fitted astrophysical parameters agree to within  $1.5\sigma$  with the values in Nielsen et al. (2020).

A major difference in the data analysis methodologies employed by the two independent studies is that Nielsen et al. (2020) removed the primary transits from the light curve prior to fitting. When considering the relatively low signal-to-noise of the data as well as the significant stellar variability in the photometry of a few percent, the atmospheric brightness modulation is the most likely of the three phase curve components to be affected by transit removal, because trimming those data removes the minima of the associated photometric variation and may induce a systematic bias in the retrieved amplitude. To

**Table 2.** Results from Phase Curve Fits

Parameter	<u>HIP 65A</u>		<u>TOI-503</u>		<u>WASP-30</u>		<u>WASP-72</u>	
	Value	Error	Value	Error	Value	Error	Value	Error
<i>Fitted Parameters</i>								
$R_p/R_*$	0.255	+0.041 -0.040	0.086	+0.040 -0.014	0.0645	+0.0010 -0.0011	0.06475	+0.00063 -0.00069
$T_0$ (BJD <sub>TDB</sub> - 2458000)	354.552123	+0.000064 -0.000067	503.08556	+0.00032 -0.00034	369.4356	+0.0028 -0.0018	412.21666	0.00029
$P$ (days)	0.9809761	+0.000037 -0.000034	3.67744	0.00015	4.15702	0.00040	2.216784	+0.000040 -0.000039
$b$	1.167	0.047	0.970	+0.063 -0.038	0.15	+0.11 -0.10	0.667	+0.037 -0.047
$a/R_*$	5.151	+0.064 -0.067	7.35	+0.61 -0.72	8.14	+0.27 -0.34	3.71	+0.17 -0.15
$\bar{f}_p$ (ppm)	...	...	...	...	...	...	52	+29 -26
$A_{\text{atm}}$ (ppm)	30.4	+8.5 -7.7	...	...	...	...	66	14
$\delta$ (°)	...	...	...	...	...	...	...	...
$A_{\text{ellip}}$ (ppm)	29.0	+7.7 -7.9	60.2	+7.4 -7.8	101	+22 -21	...	...
$A_{\text{Dopp}}$ (ppm)	...	...	30.1	+7.4 -8.5	...	...	...	...
$u_1$	0.494	+0.049 -0.053	0.28	+0.31 -0.22	0.31	+0.11 -0.14	0.17	+0.15 -0.13
$u_2$	0.159	+0.050 -0.051	0.28	+0.37 -0.20	0.18	+0.28 -0.13	0.31	+0.18 -0.20
<i>Derived Parameters</i>								
Transit depth (ppm) <sup>a</sup>	65000	+22000 -19000	7400	+8500 -2200	4160	+130 -140	4193	+83 -89
$i$ (°)	76.89	+0.62 -0.55	82.4	+0.9 -1.4	88.95	+0.73 -0.85	79.6	+1.2 -1.0
Secondary eclipse depth, $D_d$ (ppm)	...	...	...	...	...	...	118	+31 -27
Nightside flux, $D_n$ (ppm)	...	...	...	...	...	...	-15	+33 -31

Parameter	<u>WASP-100</u>		<u>WASP-111</u>		<u>WASP-122/KELT-14</u>	
	Value	Error	Value	Error	Value	Error
<i>Fitted Parameters</i>						
$R_p/R_*$	0.08393	+0.00029 -0.00031	0.08198	+0.00045 -0.00050	0.1103	0.0013
$T_0$ (BJD <sub>TDB</sub> - 2458000)	509.105439	+0.000063 -0.000066	337.13712	0.00016	503.53226	0.00014
$P$ (days)	2.8493824	+0.0000017 -0.0000016	2.310952	+0.000043 -0.000045	1.710017	+0.000031 -0.000030
$b$	0.560	+0.014 -0.015	0.691	+0.016 -0.018	0.845	+0.013 -0.014
$a/R_*$	5.382	+0.055 -0.054	4.378	+0.091 -0.084	4.388	+0.090 -0.087
$\bar{f}_p$ (ppm)	54	+12 -13	123	+31 -32	106	+56 -49
$A_{\text{atm}}$ (ppm)	49.4	+4.1 -4.2	...	...	65	+15 -16
$\delta$ (°)	14.2	4.6	...	...	...	...
$A_{\text{ellip}}$ (ppm)	...	...	...	...	...	...
$A_{\text{Dopp}}$ (ppm)	...	...	...	...	...	...
$u_1$	0.239	+0.066 -0.076	0.21	+0.11 -0.13	0.17	+0.19 -0.12
$u_2$	0.18	+0.11 -0.10	0.18	+0.17 -0.13	0.21	+0.21 -0.15
<i>Derived Parameters</i>						
Transit depth (ppm) <sup>a</sup>	7044	+48 -51	6720	+74 -82	12160	+300 -280
$i$ (°)	84.03	+0.22 -0.21	80.92	+0.42 -0.40	78.89	+0.41 -0.40
Secondary eclipse depth, $D_d$ (ppm)	102	+13 -14	123	+31 -32	172	+58 -53
Nightside flux, $D_n$ (ppm)	7	+13 -14	...	...	41	+57 -49

**Notes.**

<sup>a</sup> This parameter is calculated as  $(R_p/R_*)^2$ . For systems with a high impact parameter, this value is significantly larger than the observed transit depth.

<sup>b</sup> Constrained by priors extrapolated from values in Claret (2018):  $(u_1, u_2) = (0.50 \pm 0.05, 0.16 \pm 0.05)$ .

explore this possibility, we repeated our joint fit with the transits removed and obtained  $A_{\text{atm}} = 32.3^{+9.1}_{-8.9}$  ppm. This value is consistent with the value derived from our fit including the transits ( $30.4^{+8.5}_{-7.7}$  ppm), while being marginally closer ( $2.5\sigma$ ) to the value reported in Nielsen et al. (2020) ( $57.5 \pm 4.7$  ppm).

This test illustrates that transit trimming and ramp removal, as well as the general treatment of systematics and stellar variability, can have notable consequences in the light curve fits, particularly in datasets with inherently weak signals and relatively poor photometric precision. The *TESS* spacecraft will reobserve this system during the first year of the Extended Mission and will likely more than double the amount of available photometry, improving the precision and robustness of the phase curve fits.

#### 4.3. TOI-503

TOI-503b was the first brown dwarf discovered by the *TESS* mission (Šubjak et al. 2019) and was observed during Sector 7. This  $54 M_{\text{Jup}}$  object, listed in the *TESS* Releases as TOI-129b, orbits a metallicity 7650 K A-type star every 3.68 days. We detected strong phase curve signals corresponding to ellipsoidal distortion ( $A_{\text{ellip}} = 60.2^{+7.4}_{-7.8}$  ppm) and Doppler boosting ( $A_{\text{Dopp}} = 30.1^{+7.4}_{-8.5}$  ppm). Meanwhile, the predicted secondary eclipse depth is less than 20 ppm, and we did not measure significant values for  $\bar{f}_p$  or  $A_{\text{atm}}$ . The full list of fitted astrophysical parameters is given in Table 2.

For the other astrophysical parameters, which we allowed to vary unconstrained, we obtained values that agree with the measurements in Šubjak et al. (2019) to within  $1.5\sigma$ . The uncertainties in their work are up to 5 times smaller than ours, because they incorporated other ground-based transit observations, radial velocities, the stellar spectral energy distribution, and *Gaia* parallax into a joint fit to better constrain the limb darkening and orbital parameters. The light curve plot from our phase curve analysis is provided in Figure 2.

#### 4.4. WASP-30

WASP-30b is a  $63 M_{\text{Jup}}$   $0.95 R_{\text{Jup}}$  brown dwarf orbiting an F8V star with an orbital period of 4.16 days (Anderson et al. 2011; Triaud et al. 2013). The *TESS* spacecraft observed this system during Sector 2. In our light curve fits, we utilized priors on  $b$  and  $a/R_*$ . The only significant phase curve modulation detected was ellipsoidal distortion, and we measured a semiamplitude of  $101^{+22}_{-21}$  ppm. From separate joint fits, we obtained a  $2\sigma$  upper limit on the Doppler boosting amplitude of 37 ppm and a weak atmospheric brightness modulation signal with a semiamplitude of  $A_{\text{atm}} = 36 \pm 25$  ppm. Including these terms in the joint fit incurred significant increases to the BIC and no improvement to the AIC, indicating that the measured signals are not statistically robust. See Table 2 for the results from the lowest-BIC joint fit that includes just the ellipsoidal dis-

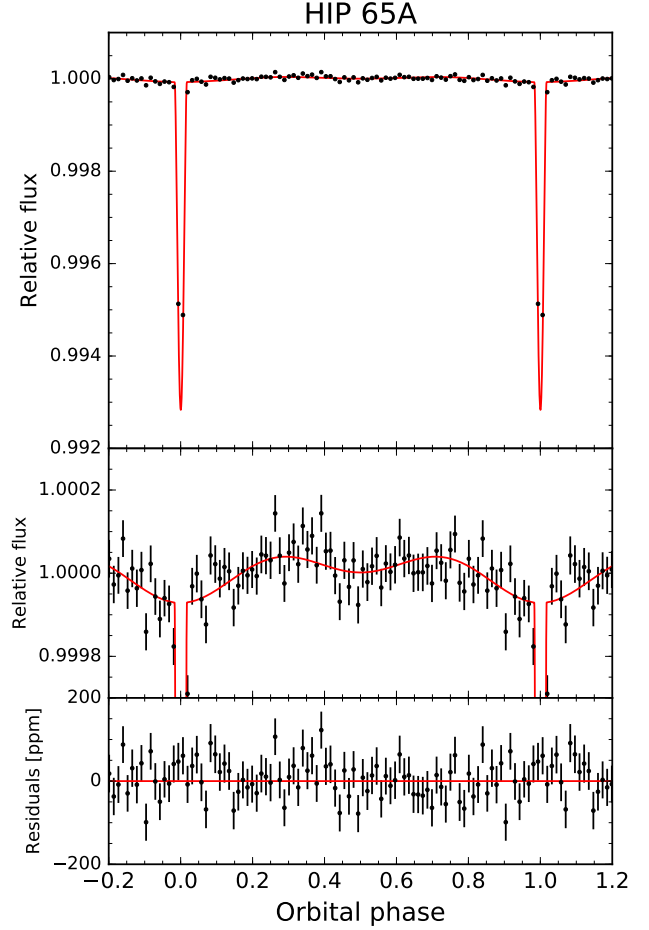


**Figure 1.** Top: systematics-removed, phase-folded *TESS* light curve of HIP 65A, binned in 18 minute intervals (black points), along with the best-fit full phase curve model (red curve). Middle: zoomed in view to show the orbital phase curve variations. We detected statistically robust signals corresponding to the atmospheric brightness modulation ( $A_{\text{atm}} = 30.4^{+8.5}_{-7.7}$  ppm) and ellipsoidal distortion ( $A_{\text{ellip}} = 29.0^{+7.7}_{-7.9}$  ppm). The full results from our joint light curve fit are listed in Table 2. Bottom: corresponding residuals from the best-fit phase curve model.

tortion term. The corresponding best-fit phase curve model and systematics-corrected *TESS* light curve are shown in Figure 3.

We derived an updated transit ephemeris:  $T_0 = 2458369.4356^{+0.0028}_{-0.0018}$  BJD<sub>TDB</sub>,  $P = 4.15702 \pm 0.00040$  days. Extrapolating the most recent literature ephemeris from Triaud et al. (2013), calculated using observations obtained in 2010, to the *TESS* epoch, we found that the transits occurred  $\sim 45$  minutes ( $3.9\sigma$ ) later than predicted. This discrepancy most likely indicates significant ephemeris deprecation over the 8 years that transpired between the *TESS* observations and the last published epoch. This target was observed for only a

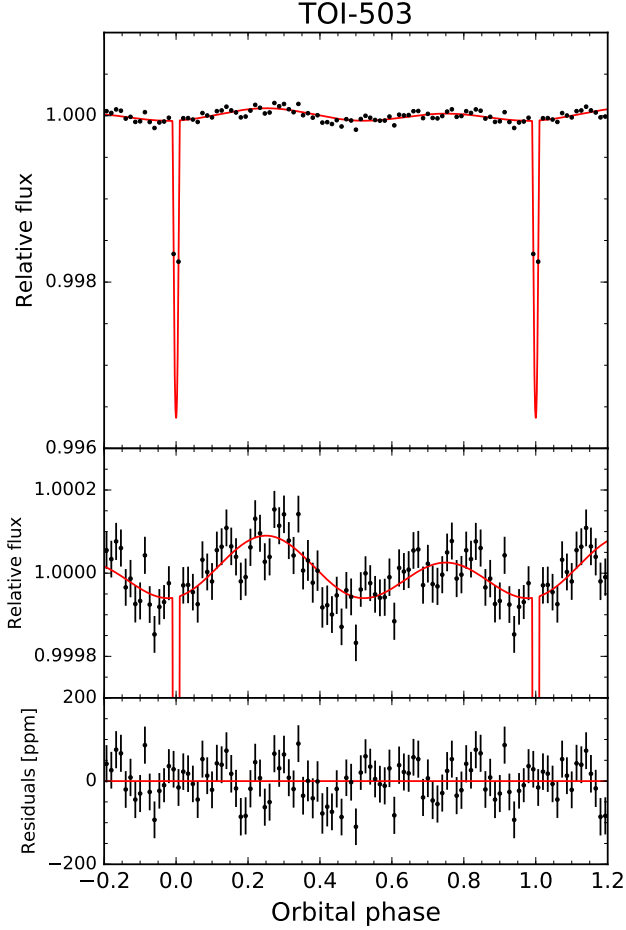


**Figure 2.** Same as Figure 1, but for TOI-503. The phase-folded light curve is binned in 70 minute intervals. Both ellipsoidal distortion and Doppler boosting phase curve signals were robustly detected in the *TESS* photometry, with measured semiamplitudes of  $60.2^{+7.4}_{-7.8}$  ppm and  $30.1^{+7.4}_{-8.5}$  ppm, respectively.

single *TESS* Sector and due to its relatively long orbital period, only six transits are contained in the light curve, resulting in relatively large uncertainties on the transit shape parameters. We obtained an impact parameter of  $b = 0.15^{+0.11}_{-0.10}$ , which is consistent with the value from [Triaud et al. \(2013\)](#):  $b = 0.10^{+0.12}_{-0.10}$ . Meanwhile, the scaled semi-major axis values  $a/R_*$  from our two analyses differ by  $1.4\sigma$ :  $8.14^{+0.27}_{-0.34}$  vs.  $8.59^{+0.09}_{-0.18}$ . The WASP-30 system will be observed again in late 2020 during the first year of the *TESS* Extended Mission, and follow-up analyses of the light curve will produce an independent transit ephemeris and determine whether there are long-term variations to the orbit of the brown dwarf due to a possible long-period companion.

#### 4.5. WASP-72

WASP-72b was discovered by [Gillon et al. \(2013\)](#) using observations collected by the WASP southern station in

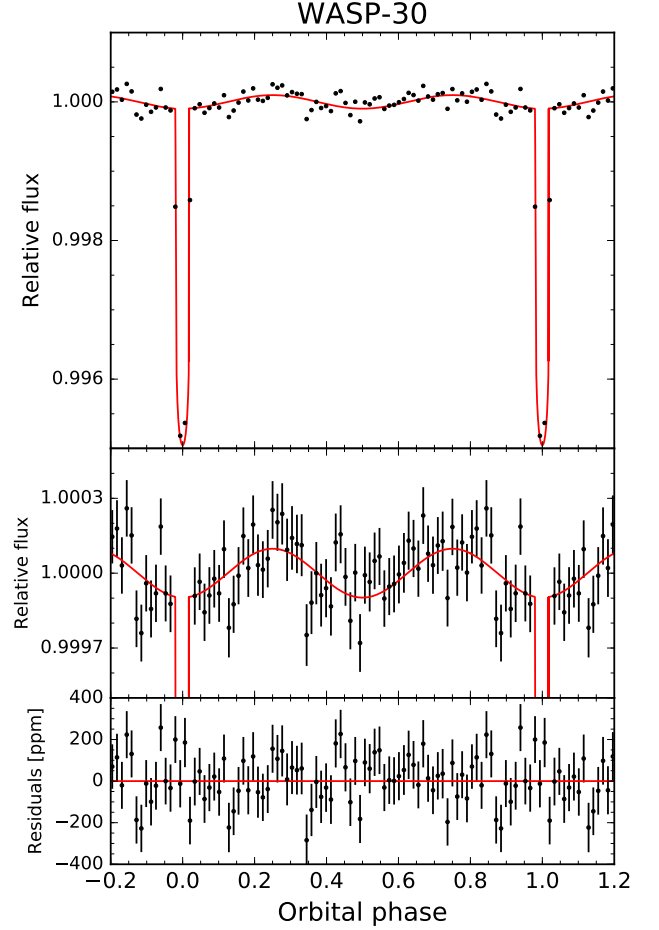


**Figure 3.** Same as Figure 1, but for WASP-30. The phase-folded light curve is binned in 80 minute intervals. The light curve shows a strong phase curve signal from the ellipsoidal distortion of the host star with a semiamplitude of  $99^{+21}_{-20}$  ppm.

2006 and 2007. The host star is a bright ( $V = 9.6$  mag), moderately evolved F7-type star with  $T_{\text{eff}} = 6250$  K,  $M_* = 1.4 M_{\odot}$ , and  $R_* = 2.0 R_{\odot}$ . The  $1.5 M_{\text{Jup}}$  companion has an orbital period of 2.22 days, and subsequent measurements of the Rossiter-McLaughlin effect revealed a sky-projected spin-orbit angle of  $-7^{+12}_{-11}$  deg ([Addison et al. 2018](#)). *TESS* observed the WASP-72 system in Sectors 3 and 4.

From the results listed in Table 2 and the light curve fit in Figure 4, we find that a prominent  $4.4\sigma$  secondary eclipse depth of  $118^{+31}_{-27}$  ppm was measured, along with a  $4.7\sigma$  atmospheric brightness modulation signal with a semiamplitude of  $66 \pm 14$  ppm. When including a phase shift in the atmospheric component in the joint fit, we derived a value that is consistent with zero at the  $0.1\sigma$  level. The nightside flux is also consistent with zero at the  $0.5\sigma$  level. Meanwhile, we obtained constraints on the orbital ephemeris ( $T_0 = 2458412.21666 \pm$

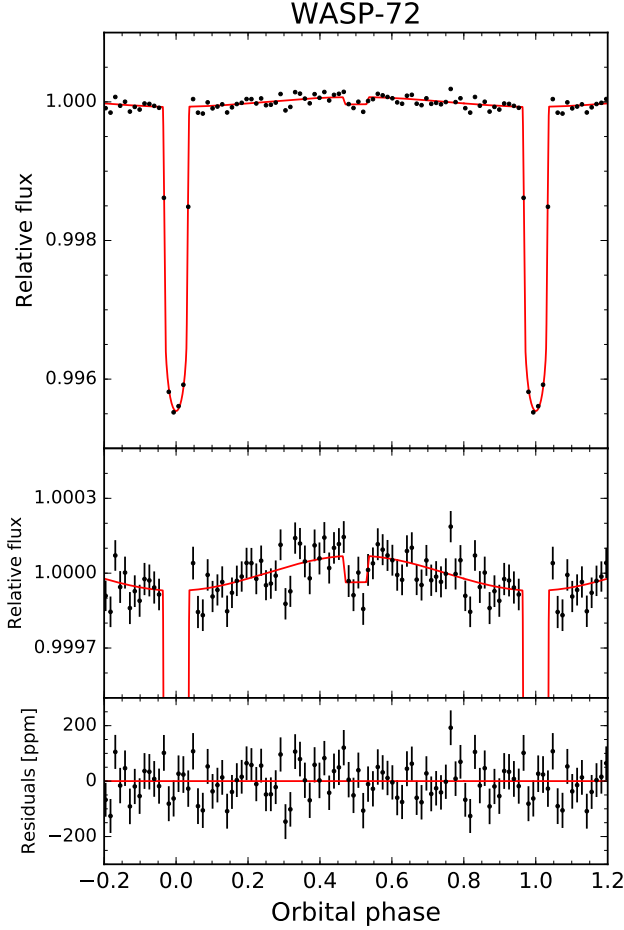


**Figure 4.** Same as Figure 1, but for WASP-72. The phase-folded light curve is binned in 43 minute intervals. Both the secondary eclipse ( $D_d = 118^{+31}_{-27}$  ppm) and the atmospheric brightness modulation ( $A_{\text{atm}} = 66 \pm 14$  ppm) were detected.

0.00029 BJD<sub>TDB</sub>,  $P = 2.216784^{+0.000040}_{-0.000039}$  d), transit shape parameters ( $b = 0.667^{+0.037}_{-0.047}$ ,  $a/R_* = 3.71^{+0.17}_{-0.15}$ ), and transit depth ( $R_p/R_* = 0.06475^{+0.00063}_{-0.00069}$ ) that significantly supersede the published values in Gillon et al. (2013) and Addison et al. (2018), with uncertainties that are as much as 4 times smaller, while being consistent with the previous values to within  $1\sigma$ .

#### 4.6. WASP-100

WASP-100b ( $2.0 M_{\text{Jup}}$ ,  $1.7 R_{\text{Jup}}$ ) orbits a solar-metallicity F2-type star ( $1.6 M_{\odot}$ ,  $2.0 R_{\odot}$ , 6900 K) every 2.85 days (Hellier et al. 2014). Follow-up observations of the Rossiter-McLaughlin effect revealed that WASP-100b is on a nearly-polar orbit ( $\lambda = 79^{+19}_{-10}$  deg; Addison et al. 2018). Located at RA=04:35:50, Dec=−64:01:37, this target lies in the *TESS* continuous viewing zone (CVZ) and was observed during all 13 Southern Sky Sectors, resulting in one year of nearly-continuous photometry.

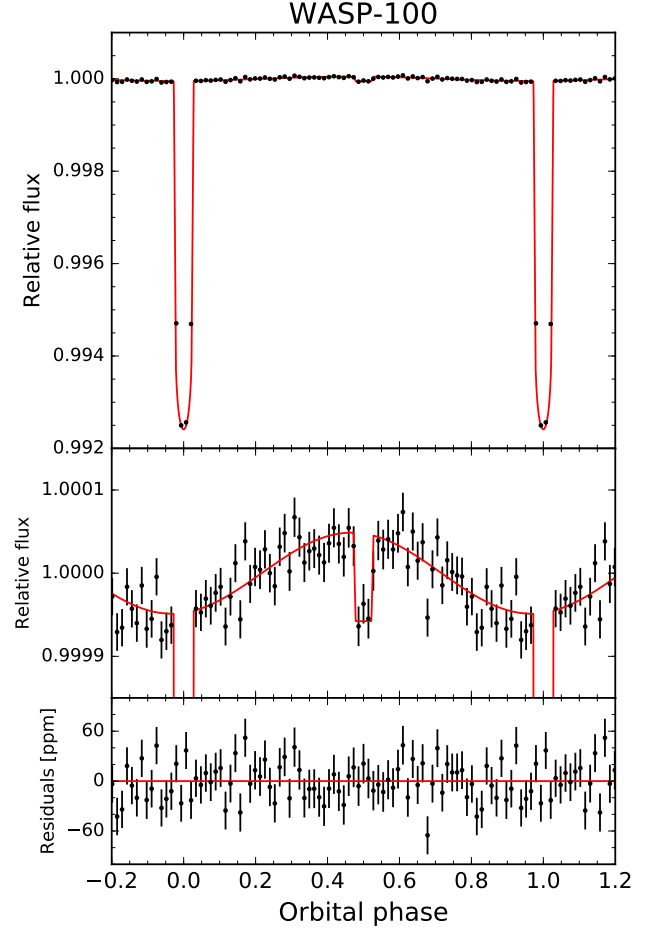


**Figure 5.** Same as Figure 1, but for WASP-100. The phase-folded light curve is binned in 56 minute intervals. Both the secondary eclipse ( $D_d = 102^{+13}_{-14}$  ppm) and atmospheric brightness modulation ( $A_{\text{atm}} = 49.4^{+4.1}_{-4.2}$  ppm) are measured at high signal-to-noise. We also detect a slight phase shift in the atmospheric brightness modulation, with the location of maximum brightness on the dayside hemisphere shifted to the east by  $14.2 \pm 4.6$ .

Due to the high volume of data, we did not use the uncorrected PDC light curves in the joint fit, because that would entail over 100 systematics parameters and incur forbiddingly large computational overheads. Instead, we followed a technique similar to the one utilized in Wong et al. (2020c) and carried out smaller joint fits of each Sector of *TESS* photometry, optimizing the orders of the detrending polynomials for all segments contained within the Sector. We then divided out the best-fit systematics model from the corresponding segment light curves, before concatenating all the detrended data segments together for the full 13-Sector joint fits; in the final joint fits, no systematics model was included.

The PDC light curves for this system are largely well-behaved, with no significant variations due to stel-

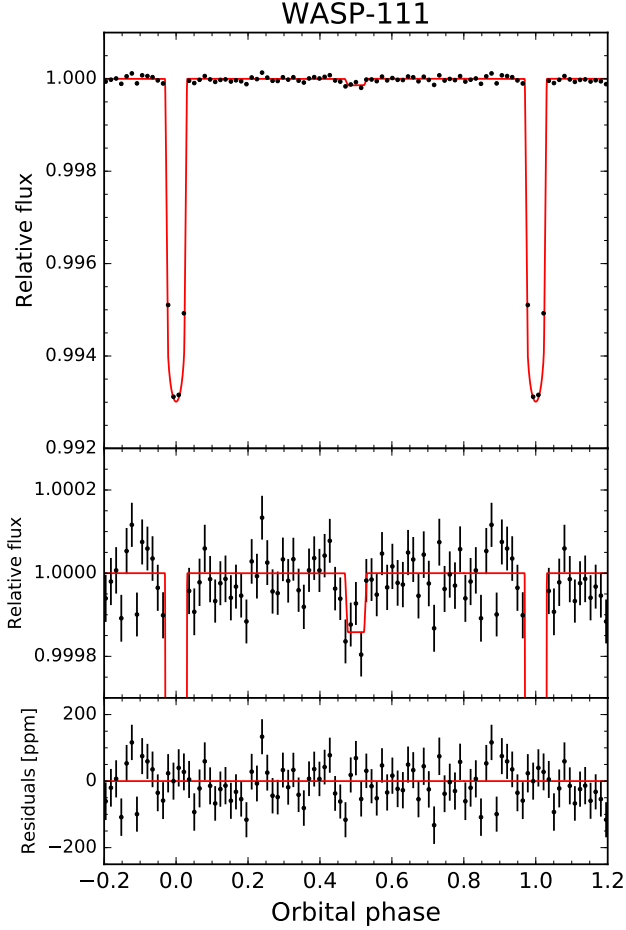


**Figure 6.** Same as Figure 1, but for WASP-111. The phase-folded light curve is binned in 44 minute intervals. The only significant signal detected in our fit is the secondary eclipse, which has a measured depth of  $133^{+30}_{-28}$  ppm.

lar variability or uncorrected instrumental systematics. Therefore, the long-term trends could be removed prior to fitting without introducing any significant biases to the resulting fitted astrophysical parameters. As an empirical test of the reliability of this detrending method, we compared the phase curve parameters from the individual Sector light curve fits and found that the values are consistent with those from the joint fit to within roughly  $2\sigma$ .

The BIC is optimized for the model fit that includes only the secondary eclipse and atmospheric brightness modulation components; meanwhile, the AIC strongly favors the addition of a phase shift in the atmospheric brightness modulation ( $\Delta\text{AIC} = -7.2$  relative to the fit without phase shift). We have chosen to present the results from our lowest-AIC fit in Table 2 and Figure 5, primarily to aid in comparison with the results of Jansen & Kipping (2020) (see below).

The long-baseline photometry of the WASP-100 system yielded exquisite updated measurements of the or-

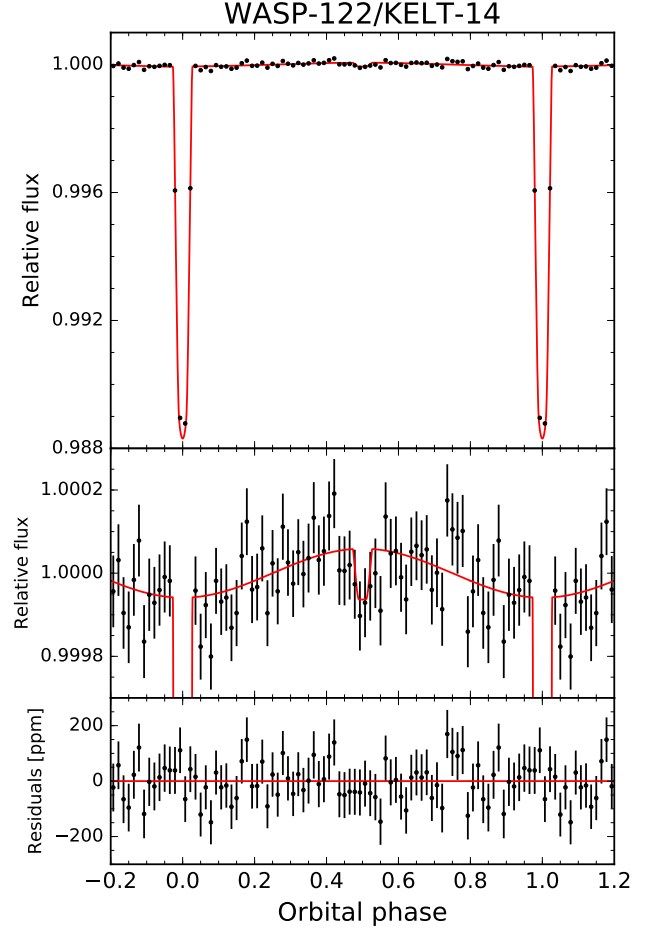


**Figure 7.** Same as Figure 1, but for WASP-122/KELT-14. The phase-folded light curve is binned in 33 minute intervals. Both the secondary eclipse ( $D_d = 172^{+58}_{-53}$  ppm) and atmospheric brightness modulation ( $A_{\text{atm}} = 65^{+15}_{-16}$  ppm) were detected in our phase curve fit.

bital ephemeris, transit shape, transit depth, and limb darkening coefficients. All of these agree with the previous literature values (Hellier et al. 2014) to well within  $1\sigma$ , with the exception of the mid-transit time  $T_0$ : our measurement is 9 min ( $1.8\sigma$ ) later than the extrapolated transit timing from the most recent published ephemeris (Addison et al. 2018). We measured a  $7.9\sigma$  secondary eclipse depth of  $102^{+13}_{-14}$  ppm and detected a very robust  $11.4\sigma$  atmospheric brightness modulation phase curve component with a semi-amplitude of  $49.4^{+4.2}_{-4.1}$  ppm; these are by far the strongest secondary eclipse and phase curve signals detected in this systematic study. The derived nightside flux is consistent with zero, and we obtained a marginal phase shift in the brightness modulation of  $\delta = 14.2 \pm 4.6^\circ$ .

Including the ellipsoidal distortion term resulted in a null detection, with  $A_{\text{ellip}} = 3 \pm 4$  ppm. Given the inherent degeneracy between a phase shift in the atmospheric brightness modulation component and Doppler

boosting, we calculated the predicted semiamplitude of the latter signal, following the methodology described in Sections 3 and 5.1, and obtained  $2.1 \pm 0.1$  ppm. This value is small compared to the amplitude of the atmospheric brightness modulation, and as such, our phase shift measurement is not significantly affected by the presence of Doppler boosting.

#### 4.6.1. Comparison with Jansen & Kipping (2020)

Jansen & Kipping (2020) presented an independent phase curve analysis of the full 13-Sector WASP-100 dataset. Their fits of the secondary eclipses alone yielded a depth of  $100 \pm 14$  ppm, consistent with our result to well within  $1\sigma$ . From fitting the phase curve, they reported an eastward offset in the region of maximum dayside brightness of  $28^\circ \pm 9^\circ$ , in broad agreement with our measured value  $14^\circ 2 \pm 4^\circ 6$ .

The treatment of the ellipsoidal distortion signal in Jansen & Kipping (2020) differs significantly from our approach. Instead of retrieving the magnitude of the associated sinusoidal term from an unconstrained fit, they applied a prior on the amplitude derived from propagating the measured properties of the system through the theoretical formulation described in Equation (8). The resultant value from their fit is  $12.2^{+3.3}_{-3.2}$  ppm, roughly  $1.8\sigma$  larger than our nondetection of  $3 \pm 4$  ppm.

Jansen & Kipping (2020) reported a peak-to-peak brightness variation of  $73 \pm 9$  ppm, whereas we measured  $2A_{\text{atm}} = 99 \pm 8$ , roughly  $2.2\sigma$  larger. We note that in their phase curve analysis, they removed both the primary transit and the secondary eclipse (roughly 20% of the time series altogether). Additionally, they phase-folded and binned the data and detrended the light curves prior to fitting, similar to the approach used in the analysis of the HIP 65A phase curve in Nielsen et al. (2020). Trimming away the data points spanning the two conjunctions removes the regions near both the maxima and the minima of the characteristic atmospheric brightness modulation, and, as discussed in Section 4.2, this may affect the measured amplitude and phase shift, particularly given the relatively low signal-to-noise of the *TESS* photometry for this system.

Follow-up studies of WASP-100 using data from the *TESS* Extended Mission will help better constrain the phase shift in the atmospheric brightness component and more robustly measure the day-night brightness contrast.

#### 4.7. WASP-111

WASP-111b is a  $1.8 M_{\text{Jup}}$ ,  $1.4 R_{\text{Jup}}$  hot Jupiter that orbits its  $V = 10.3$  mag 6400 K F5 host star every 2.31 days (Anderson et al. 2014). Measurements of the Rossiter-McLaughlin effect indicate a prograde orbit with a sky-projected stellar obliquity of  $\lambda = -5^\circ \pm 16^\circ$ . *TESS* observed the WASP-111 system during Sector 1. No significant phase curve components were detected in our joint fits. The secondary eclipse depth

is  $123^{+32}_{-31}$  ppm. We obtained improved values for transit depth, orbital ephemeris, and transit shape parameters that agree with the previously published results from the discovery paper to within  $1\sigma$ . The full list of fitted parameters is given in Table 2; the phase-folded, systematics-corrected light curve and best-fit model are shown in Figure 6.

#### 4.8. WASP-122/KELT-14

This  $1.2 M_{\text{Jup}}$ ,  $1.5 R_{\text{Jup}}$  hot Jupiter on a 1.71 day orbit was discovered independently by the WASP consortium (as WASP-122b; Turner et al. 2016) and the Kilodegree Extremely Little Telescope survey (as KELT-14b; Rodriguez et al. 2016). The metal-rich G4-type host star has  $T_{\text{eff}} = 5800$  K,  $M_* = 1.2 M_\odot$ , and  $R_* = 1.2 R_\odot$ . Our analysis of the *TESS* Sector 7 light curve revealed a  $3.2\sigma$  secondary eclipse depth of  $172^{+59}_{-53}$  ppm and a  $4.1\sigma$  atmospheric brightness modulation semiamplitude of  $65^{+15}_{-16}$  ppm. As in the case of WASP-72b and WASP-100b, the corresponding night-side flux is consistent with zero, and no significant phase shift in the brightness modulation was detected. All other fitted orbital ephemeris and transit shape parameters are consistent to better than the  $1.5\sigma$  level with the results of Turner et al. (2016) and Rodriguez et al. (2016), with comparable relative uncertainties. See Table 2 and Figure 7.

### 5. DISCUSSION

#### 5.1. Mutual gravitational interaction

We detected phase curve signals attributed to ellipsoidal distortion and/or Doppler boosting in three systems: HIP 65A (Section 4.2), TOI-503 (Section 4.3), and WASP-30 (Section 4.4). Comparisons of the observed amplitudes from our light curve analysis with the predictions from theoretical modeling provide an empirical test of the commonly used simple models for describing those phenomena.

For ellipsoidal distortion signals, we combined measurements of  $a/R_*$  and  $i$  derived from our phase curve analysis with literature values for the mass ratio  $M_p/M_*$  to compute the predicted modulation semiamplitudes using Equation (8). For the limb-darkening and gravity-darkening coefficients in the pre-factor  $\alpha_{\text{ellip}}$ , we took the tabulated values from Claret (2017) for the nearest available combination of stellar parameters. To propagate the uncertainties on the system parameters to the prediction, we used a standard Monte Carlo sampling method and drew values from the individual Gaussian distributions based on the measurement uncertainties.

For HIP 65A, the predicted ellipsoidal distortion amplitude is  $40 \pm 2$  ppm, which is consistent with the measured amplitude of  $29.0^{+7.7}_{-7.9}$  ppm at the  $1.3\sigma$  level. The measured effective temperature of TOI-503 is  $7650 \pm 160$  K and lies in a region where the model-generated gravity-darkening coefficients vary significantly and non-

monotonically across a relatively narrow range of temperatures. To account for the large corresponding uncertainty in  $g$ , we used the range of values for temperatures spanning 7500–7800 K:  $0.1174 < g < 0.5684$ . The resultant spread in the predicted ellipsoidal distortion amplitudes is 58–131 ppm. Our measured amplitude of  $60.2^{+7.4}_{-7.8}$  ppm agrees well with the lower end of this range. The predicted ellipsoidal distortion amplitude for WASP-30 is  $118^{+26}_{-20}$  ppm when using the values for  $b$  and  $a/R_*$  measured in our fits (Table 2); when assuming the more precise literature values from Anderson et al. (2011), the predicted amplitude is  $85^{+5}_{-4}$  ppm. Both of these predictions are consistent with our measured amplitude of  $101^{+22}_{-21}$  ppm at better than the  $1\sigma$  level.

The theoretical model for the Doppler boosting signal is given in Equation (10). Assuming the host star is a blackbody and substituting in the expression for the RV semiamplitude for a circular orbit, we can analytically calculate the prefactor  $\alpha_{\text{Dopp}}$  (defined in Equation (11)) and express the Doppler boosting amplitude as (e.g., Shporer 2017)

$$A_{\text{Dopp}} = \sin i \left[ \frac{2\pi G}{Pc^3} \frac{q^2 M_p}{(1+q)^2} \right]^{\frac{1}{3}} \left\langle \frac{xe^x}{e^x - 1} \right\rangle_{\text{TESS}}, \quad (12)$$

where  $x \equiv hc/kT_{\text{eff}}\lambda$ ,  $q \equiv M_p/M_*$ , and the term in the angled brackets is integrated over the *TESS* bandpass. Using the values for  $M_p$ ,  $M_*$ , and  $T_{\text{eff}}$  from the literature and the values for  $P$  we obtained in our *TESS* light curve fits, we calculated predicted Doppler boosting amplitudes of  $10.4 \pm 0.3$  ppm,  $41 \pm 1$  ppm, and  $71 \pm 2$  ppm for HIP 65A, TOI-503, and WASP-30, respectively. For HIP 65A, we measured a marginal Doppler boosting signal with  $A_{\text{Dopp}} = 18.4 \pm 7.0$  ppm, consistent with the predicted amplitude. Likewise for TOI-503, our measured amplitude of  $30.1^{+7.4}_{-8.5}$  ppm agrees with the prediction at the  $1.5\sigma$  level.

For WASP-30, we did not detect a statistically significant Doppler boosting signal. Given the uncertainty on  $A_{\text{Dopp}}$  from our fit (26 ppm; Section 4.4), the predicted signal of 71 ppm would be a roughly  $2.7\sigma$  detection. Taking into account breaks in data collection between spacecraft orbits and data points flagged by the SPOC pipeline, the *TESS* light curve of WASP-30 contains only four uninterrupted orbital cycles (transit to transit). The inclusion of more data, e.g., when the system is revisited during the *TESS* Extended Mission, will help better constrain the amplitude of this phase curve component and more robustly determine whether the predicted Doppler boosting signal is present in the photometry.

For the three systems analyzed in this paper with significant phase curve contributions from the mutual star–planet gravitational interaction, the measured signals are broadly consistent with theoretical predictions. Among the systems with previously published *TESS* phase curve studies, WASP-18 was an exem-

plary target for which both ellipsoidal distortion and Doppler boosting signals were detected at relatively high signal-to-noise (Shporer et al. 2019); in that case, both measured amplitudes agreed well with the predictions. In contrast, the phase curve of KELT-9 shows an anomalous ellipsoidal distortion signal that is shifted in time relative to the expected phase, indicating possible secondary effects due to the stellar dynamical tide excited by the orbiting planet or additional contributions to the overall photometric modulation at the first harmonic of the orbital phase due to time-varying stellar illumination across the planet’s near-polar orbit (Wong et al. 2020d).

Looking more broadly at phase curve studies from the *Kepler* era, we find numerous systems for which the measured ellipsoidal distortion signals diverge from the corresponding theoretical predictions. Examples include KOI-964, a transiting hot white dwarf system for which the theoretical model underestimates the observed ellipsoidal distortion amplitude (Wong et al. 2020c), and KOI-74, another transiting white dwarf system where the opposite deviation in the measured ellipsoidal distortion signal was reported (e.g., van Kerkwijk et al. 2010; Ehrenreich et al. 2011; Bloemen et al. 2012). Many of these discrepant systems, including KELT-9, KOI-74, and KOI-964, contain hot primary stars, suggesting that the nonconvective nature of the hosts may be affecting the tidal response to the orbiting companion’s gravitational potential. Detailed numerical modeling of hot stars (e.g., Pfahl et al. 2008; Burkart et al. 2012) has revealed that the dynamical tide can induce significant deviations in the observed ellipsoidal distortion signal from the classical theoretical predictions (i.e., Equation (8)) that assume only the equilibrium tide.

TOI-503 joins the list of binary systems with hot primary stars that have detected phase curve modulations due to ellipsoidal distortion and Doppler boosting. Future follow-up spectroscopic studies of the host star can yield improved measurements of the stellar effective temperature, which in turn translate into better constraints on the limb- and gravity-darkening coefficients, and more precise estimates of the gravitational phase curve amplitudes. Combining these results with additional *TESS* photometry from the Extended Mission will allow us to determine whether this system’s phase curve variability deviates significantly from theoretical predictions.

## 5.2. Brightness temperatures and albedos

The secondary eclipse depth at visible wavelengths contains contributions from reflected starlight as well as thermal emission. Due to the composite nature of this quantity, there is an inherent degeneracy between the dayside temperature,  $T_{\text{day}}$ , and the geometric albedo of the atmosphere in the observed bandpass,  $A_g$ . More specifically, these parameters are negatively correlated, because a decrease in the dayside temperature lowers

**Table 3.** Dayside Brightness Temperatures and Albedos Derived from *TESS* and *Spitzer*/IRAC 3.6 and 4.5  $\mu\text{m}$  Secondary Eclipses

Planet	$D_{d,\text{TESS}}$ (ppm) <sup>a</sup>	$D_{d,3.6}$ (ppm) <sup>a</sup>	$D_{d,4.5}$ (ppm) <sup>a</sup>	$T_{\text{day}}$ (K)	$A_g$ <sup>b</sup>
WASP-36b	$120^{+100}_{-80}$	$914 \pm 578$	$1953 \pm 544$	$1370^{+150}_{-170}$	$0.23 \pm 0.19$
WASP-43b	$170^{+80}_{-70}$	$3773 \pm 138$	$3866 \pm 195$	$1632 \pm 46$	$0.14 \pm 0.07$
WASP-46b	$110^{+110}_{-80}$	$1360 \pm 701$	$4446 \pm 589$	$1820 \pm 120$	$< 0.48$
WASP-64b	$230^{+120}_{-110}$	$2859 \pm 270$	$2071 \pm 471$	$1878^{+95}_{-96}$	$0.39 \pm 0.24$
WASP-77Ab	$55^{+20}_{-18}$	$2016 \pm 94$	$2487 \pm 127$	$1855 \pm 33$	$0.06 \pm 0.04$
WASP-78b	$220^{+80}_{-90}$	$2001 \pm 218$	$2013 \pm 351$	$2470^{+180}_{-170}$	$< 0.65$
WASP-100b	$102^{+13}_{-14}$	$1267 \pm 98$	$1720 \pm 119$	$2306^{+73}_{-74}$	$0.26 \pm 0.07$
WASP-18b	$341^{+17}_{-18}$	$3037 \pm 62$	$4033 \pm 97$	$3095 \pm 52$	$< 0.02$
WASP-19b	$473^{+131}_{-106}$	$5015 \pm 175^c$	$5343 \pm 318^c$	$2141 \pm 52$	$0.19 \pm 0.08$
WASP-121b	$534^{+42}_{-43}$	$3685 \pm 114$	$4684 \pm 121$	$2438 \pm 49$	$0.27 \pm 0.04$

**Notes.**

<sup>a</sup> Secondary eclipse depths measured in the *TESS* bandpass and the 3.6 and 4.5  $\mu\text{m}$  *Spitzer*/IRAC bandpasses, in parts-per-million. Most of the *Spitzer* eclipse depth values come from Garhart et al. (2019), except for the 4.5  $\mu\text{m}$  eclipse depth for KELT-9b, which is taken from Mansfield et al. (2019). The depths for WASP-36b and WASP-77Ab have been corrected for contamination from nearby sources.

<sup>b</sup> For marginal cases,  $2\sigma$  upper limits are provided.

<sup>c</sup> Error-weighted averages of the two eclipse depths in each band from Garhart et al. (2019).

the contribution from thermal emission, which in turn requires a larger fraction of incident starlight to be reflected.

In previous systematic studies of secondary eclipses for transiting exoplanet systems observed by *Kepler* (e.g., Esteves et al. 2013, 2015; Angerhausen et al. 2015), geometric albedos were derived by fixing the dayside temperatures to values calculated under certain assumptions on the extent of heat redistribution across the planets’ surfaces, e.g., homogeneous reradiation or dayside redistribution only. Therefore, the calculations were not fully self-consistent, and as a result, the derived albedo values do not constitute direct measurements.

To break the degeneracy between dayside temperature and albedo, we must include secondary eclipse depths measurements at longer wavelengths, where the relative contribution from the planet’s thermal emission is significantly larger. Garhart et al. (2019) carried out a uniform analysis of secondary eclipse light curves obtained in both the 3.6 and 4.5  $\mu\text{m}$  bandpasses of the *Spitzer*/IRAC instrument and computed eclipse depths for several dozen exoplanets. Among the 19 systems we analyzed in this paper, 7 have eclipse depths measured in all three bandpasses (*TESS*, 3.6  $\mu\text{m}$ , and 4.5  $\mu\text{m}$ ); these include 6 systems for which only marginal secondary eclipse detections were obtained (Section 4.1). These planets are listed in Table 3. For WASP-36b and WASP-77Ab, the *Spitzer* eclipse depths have been corrected for contamination to the extracted photometry due to nearby sources on the detector, as calculated by Garhart et al. (2019); as discussed in Section 2.1, the *TESS* PDC light curves have been corrected for contam-

ination by the SPOC pipeline, and the resulting eclipse depth measurements do not need to be adjusted.

We utilized Equation (6) to simultaneously fit all three eclipse depths and obtain self-consistent measurements of the dayside brightness temperature and *TESS*-band geometric albedo. In order to straightforwardly propagate the uncertainties in stellar properties when calculating  $T_{\text{day}}$  and  $A_g$ , we calculated the integrated stellar flux in the three bandpasses for a grid of PHOENIX stellar models (Husser et al. 2013) spanning the ranges  $T_{\text{eff}} = [3000, 7500]$  K,  $\log g = [3.50, 5.00]$ , and  $[\text{Fe}/\text{H}] = [-1.0, +1.0]$  and constructed best-fit polynomial functions that we subsequently sampled in a Monte Carlo fashion when simultaneously fitting for  $T_{\text{day}}$  and  $A_g$ . For the orbiting companion, we assumed a blackbody spectrum. Garhart et al. (2019) calculated dayside brightness temperatures separately for the 3.6 and 4.5  $\mu\text{m}$  eclipse depths and found a weak correlation between increasing equilibrium temperature and increasing brightness temperature ratio between the two *Spitzer* bands. This suggests a possible systematic deviation between the true emission spectra and that of isothermal blackbodies in the infrared. Nevertheless, for all of the planets we analyzed in this paper, all three eclipse depths lie well within  $2\sigma$  of the best-fit model spectra.

We computed the posterior distributions of  $T_{\text{day}}$  and  $A_g$  using *emcee* (Foreman-Mackey et al. 2013), with  $R_p/R_*$ ,  $a/R_*$ ,  $T_{\text{eff}}$ ,  $\log g$ , and  $[\text{Fe}/\text{H}]$  as additional parameters constrained by Gaussian priors. The median and  $1\sigma$  uncertainties for  $R_p/R_*$  and  $a/R_*$  were taken from the results of our *TESS* light curve analysis, while constraints on  $T_{\text{eff}}$ ,  $\log g$ , and  $[\text{Fe}/\text{H}]$  were taken from the respective discovery papers (see citations listed in

Section 3). The resultant dayside brightness temperature and geometric albedo measurements are listed in Table 3; in marginal cases where the derived geometric albedo is less than  $1\sigma$  above zero, we provide  $2\sigma$  upper limits.

In addition to the targets we analyzed in this paper, we also include the analogously-calculated dayside brightness temperatures and geometric albedos for other systems with previously published *TESS* phase curves as well as *Spitzer* secondary eclipses at both 3.6 and 4.5  $\mu\text{m}$ : WASP-18b (Shporer et al. 2019), WASP-19b (Wong et al. 2020b), and WASP-121b (Bourrier et al. 2019; Daylan et al. 2019). To ensure maximum uniformity in this analysis, we only utilized available 3.6 and 4.5  $\mu\text{m}$  secondary eclipse depths from Garhart et al. (2019), even if measurements at other wavelengths are available in the literature. In the case of WASP-19b, there are two pairs of 3.6 and 4.5  $\mu\text{m}$  eclipse measurements; the independent eclipse depth measurements in each band are self-consistent to within  $\sim 1.1\sigma$ , and we computed the error-weighted average eclipse depth in each band for use in our analysis.

For WASP-43b, Keating & Cowan (2017) likewise assumed an isothermal blackbody for the planet’s emission spectrum and obtained  $T_{\text{day}} = 1483 \pm 10$  K and  $A_g = 0.24 \pm 0.01$  from a combined analysis of *Spitzer* and *HST*/WFC3 eclipse depths; the high-precision WFC3 data points provided for the exquisite precision in their retrieved parameter values. We note that their analysis utilized *Spitzer* eclipse depths from the analysis of Stevenson et al. (2017), which measured a significantly lower 3.6  $\mu\text{m}$  eclipse depth of  $3230 \pm 60$  ppm. This explains the higher brightness temperature and lower geometric albedo we obtained.

Meanwhile, the albedo measurements we obtained for WASP-18b and WASP-19b here are consistent with the constraints derived from previous analyses that utilized additional eclipse depths at other wavelengths and carried out more detailed modeling of the planet’s atmosphere:  $A_g < 0.048$  ( $2\sigma$ ) for WASP-18b (Shporer et al. 2019) and  $A_g = 0.16 \pm 0.04$  for WASP-19b (Wong et al. 2020b). For WASP-100b, Jansen & Kipping (2020) derived the geometric albedo from the phase curve without utilizing the *Spitzer* secondary eclipses, instead using a thermal energy balance model to retrieve the Bond albedo and day-night heat recirculation and assuming Lambertian scattering. Their value of  $A_g = 0.16^{+0.04}_{-0.03}$  is consistent with ours at the  $1.2\sigma$  level.

Only a handful of other exoplanets have direct optical geometric albedo measurements or upper limits in the literature. These include HD 189733b ( $< 0.12$  across 450–570 nm; Evans et al. 2013), HD 209458b ( $0.038 \pm 0.045$ ; Rowe et al. 2008), Kepler-7b ( $0.35 \pm 0.02$ ; Demory et al. 2013), WASP-12b (97.5% confidence upper limit at 0.064; Bell et al. 2017), and TrES-2b ( $0.014 \pm 0.003$ ; Barclay et al. 2012). The significant body of new direct geometric albedo constraints pre-

sented here underscores the importance of *TESS* and the synergy with *Spitzer* in broadening the picture of exoplanet reflectivity at visible wavelengths. Future analyses of targets in the Northern Sky and repeated observation of targets during the Extended Mission promise to further expand upon these results and refine existing albedo values.

### 5.3. Exploring trends in geometric albedo

By quantifying the reflectivity of a planet’s dayside hemisphere, the geometric albedo is an important diagnostic tool for probing the presence of clouds on exoplanets. The study of exoplanet clouds is a rich field, and extensive theoretical work has produced increasingly complex models for describing the microphysics of cloud formation as well as the interplay between incident starlight, atmospheric composition, temperature-pressure profiles, and three-dimensional heat transport (see, for example, reviews by Marley et al. 2013 and Helling 2018). At the same time, a diverse range of exoplanets have been intensively observed in reflected, transmitted, and emitted light, revealing that clouds are a common feature on exoplanets (e.g., Sing et al. 2016). As numerical models, observation techniques, and telescope capabilities continue to advance, the search for population-wide trends linking the presence and properties of clouds to other fundamental planetary and stellar parameters will provide crucial empirical tests of our current understanding of exoplanet clouds.

Having obtained a new set of uniformly-derived visible geometric albedos, we briefly explored the possibility of emergent trends within this dataset. We carried out linear fits with MCMC to various combinations of stellar and planetary parameters with plausible relevance to cloud formation, including geometric albedo  $A_g$ , dayside equilibrium temperature  $T_{\text{eq}} \equiv T_* \sqrt{R_*/2a}$ , dayside brightness temperature  $T_{\text{day}}$ , planetary surface gravity  $\log g_p$ , and stellar metallicity [Fe/H]. All statistically-significant trends are shown in Figure 8. No significant correlation was found between  $A_g$  and [Fe/H]; meanwhile, planetary metallicity measurements were not available for most targets on our list.

Condensate clouds form when the local temperature-pressure profile crosses the condensation curve of a particular cloud species. As such, the temperature across the dayside hemisphere is expected to be the primary factor in controlling the formation and extent of clouds and, by extension, the optical geometric albedo. Indeed, when removing the outlier WASP-18b from the fit, we find a  $3.2\sigma$  positive correlation between  $T_{\text{day}}$  and  $A_g$  (see Figure 8 panel a). Because we simultaneously calculated these two parameters in our joint *TESS* and *Spitzer* secondary eclipse depth fits, each individual pair of  $(T_{\text{day}}, A_g)$  values is mutually correlated. Therefore, we also probed the relationship between  $A_g$  and  $T_{\text{eq}}$  (a quantity that only depends on the stellar effective temperature and the scaled orbital semi-major axis) and

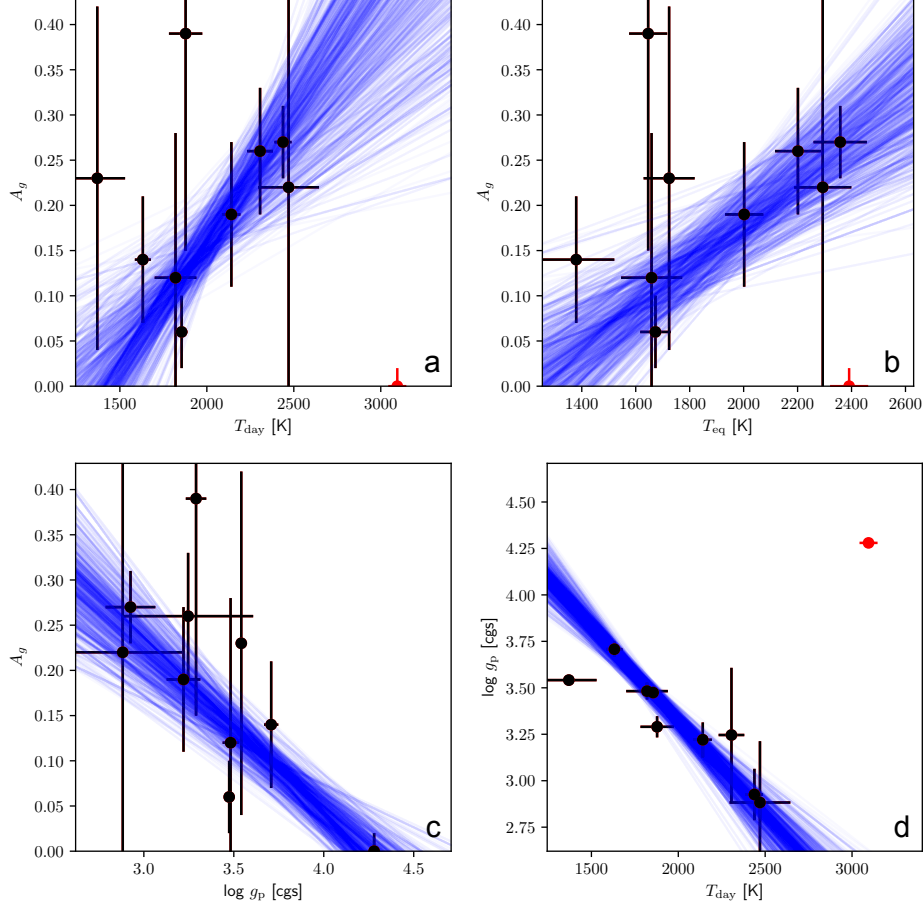


**Figure 8.** Panel a: plot of measured *TESS*-band geometric albedo  $A_g$  versus dayside brightness temperature  $T_{\text{day}}$ . We found a significant  $3.2\sigma$  correlation when removing the outlier WASP-18b (marked in red). Panel b: same as panel a, but with dayside equilibrium temperature  $T_{\text{eq}}$  on the abscissa, showing a similar positive trend. Panel c: plot of  $A_g$  vs. planetary  $\log g$ , demonstrating a strong  $6.2\sigma$  negative correlation. Panel d: the negative correlation between  $\log g$  and  $T_{\text{day}}$  ( $7.1\sigma$ ), reflecting the systematically inflated radii of highly-irradiated hot Jupiters.

likewise found a  $3.3\sigma$  correlation (see Figure 8 panel b), demonstrating that the observed trend is not contingent upon the methods used to derive the parameter values. WASP-18b is an outlier in both dayside temperature (an extreme ultra-hot Jupiter) and planet mass ( $M_p \sim 10 M_J$ , roughly an order of magnitude larger than the rest of the targets, while having a similar radius to other hot Jupiters).

We also found a robust ( $6.2\sigma$ ) correlation between  $A_g$  and  $\log g_p$  across all planets in our dataset (see Figure 8 panel c). It is expected that the planet’s surface gravity has some systematic effect on the presence and behavior of clouds in exoplanet atmospheres. For example, this property affects the atmospheric scale height, the shape of the temperature-pressure profile, and the efficiency of vertical transport processes, which in turn can influence the vertical extent, particle size distribution, and overall opacity of the clouds (e.g., Cooper et al. 2003; Ackerman & Marley 2001; Marley et al. 2012). We

note, however, that there is a very strong ( $7.1\sigma$ ) negative correlation between  $\log g_p$  and  $T_{\text{day}}$  in our dataset when removing WASP-18b (see Figure 8 panel d), reflecting the well-known irradiation-radius dependence seen across the most highly-irradiated hot Jupiters (e.g., Laughlin et al. 2011; Enoch et al. 2012). Therefore, we cannot confirm an independent fundamental trend between  $A_g$  and  $\log g_p$  from these data.

Earlier studies using *Kepler* secondary eclipse measurements have also searched for correlations between  $A_g$  and other system parameters (e.g., Heng & Demory 2013; Angerhausen et al. 2015; Esteves et al. 2015). Esteves et al. (2015) reported a similar trend between  $A_g$  and  $T_{\text{eq}}$  across a comparable range of temperatures to the one we report in Figure 8. One important distinction to make is that these earlier *Kepler* albedos did not self-consistently account for the contribution of the planets’ thermal flux in the *Kepler* bandpass, given that they were computed in the absence of longer-wavelength

secondary eclipse measurements. In most cases, an apparent geometric albedo was reported, which was derived without removing any thermal emission contribution from the secondary eclipse depth.

Parmentier et al. (2016) compiled the body of published *Kepler* apparent albedos and carried out comparisons with reflectivity curves generated by a forward model for a range of condensate species. They found that silicate clouds (in particular, MnS and MgSiO<sub>3</sub>), combined with a low-temperature cold trap that induces condensate rain-out below  $T_{\text{eq}} \sim 1600$  K, can largely reproduce the observed trend in albedos for planets with  $T_{\text{eq}} < 2000$  K. Meanwhile, the overall systematic increase in apparent albedo with rising dayside temperature, especially at  $T_{\text{eq}} > 2000$  K, was attributed to the increasing fraction of thermally emitted light in the planets' total dayside flux in the bandpass.

In our study, we have, to first order, corrected the reported albedos for the thermal component. Although the sample size is small, the tentative positive correlation between  $A_g$  and  $T_{\text{day}}$  suggests that there is indeed a systematic increase in the measured geometric albedos of hot Jupiters at dayside temperatures exceeding 2000 K. In other words, the previously reported rise in apparent geometric albedo with increasing dayside temperature cannot be explained simply by the contribution of the planets' blackbody thermal emission in the visible.

At these temperatures, all of the major silicate condensates are expected to be in the vapor phase, so the high albedo values must be caused by different molecular species. Recent work combining microphysical cloud models with three-dimensional general circulation models has shown that clouds composed of some of the most refractory molecules, TiO<sub>2</sub> and Al<sub>2</sub>O<sub>3</sub>, can survive across the dayside hemisphere of exoplanets with dayside temperatures up to 1800 K (Powell et al. 2019). While these condensates are unable to form clouds near the substellar point for hotter planets, they may still condense near the limbs and the poles, where the temperatures are significantly cooler than the overall dayside brightness temperature. Further numerical modeling is needed to probe whether such partial cloud coverage can yield enough reflectivity to explain the high geometric albedos of planets above  $T_{\text{day}} = 2000$  K.

Another plausible explanation for this albedo trend is enhanced thermal emission due to the presence of an additional opacity sources. Optical absorbers such as TiO and VO can strongly heat the atmosphere and induce temperature inversions, as has been seen on several ultra-hot Jupiters, such as WASP-121b (e.g., Parmentier et al. 2018; Daylan et al. 2019). Other possible sources of heating for the most highly-irradiated planets include the continuum opacity of H<sup>+</sup>, which forms from the dissociation of H<sub>2</sub> (e.g., Arcangeli et al. 2018), and metallic gases composed of Fe and Mg, which are expected to be present in extremely irradiated hot Jupiters (Lothringer

et al. 2018). The extra heating due to these opacity sources leads to a systematic deviation in the thermal emission spectrum at optical wavelengths from that of a simple blackbody, inflating the geometric albedo values we computed in the *TESS* bandpass.

## 6. SUMMARY

We have presented the results from our systematic study of *TESS* phase curves of known short-period transiting systems with substellar companions observed in Sectors 1–13, encompassing the first year of the *TESS* Primary Mission. After selecting for targets with likely detectable phase curve signals, we carried out a uniform analysis of 19 systems. The main findings of our work are summarized below:

- No significant phase curve signals were found for 12 systems: HATS-24, WASP-4, WASP-5, WASP-36, WASP-43, WASP-46, WASP-64, WASP-77A, WASP-78, WASP-82, WASP-142, and WASP-173A. We reported marginal secondary eclipse depth measurements or upper limits for these planets in Table 1.
- We detected statistically significant secondary eclipse depths for WASP-72b ( $118^{+31}_{-27}$  ppm), WASP-100b ( $102^{+13}_{-14}$  ppm), WASP-111b ( $133^{+30}_{-28}$  ppm), and WASP-122b/KELT-14b ( $172^{+58}_{-53}$  ppm).
- Of these four planets, WASP-72b, WASP-100b, and WASP-122b/KELT-14b show atmospheric brightness modulation, with measured semi-amplitudes of  $66 \pm 14$  ppm,  $49.4^{+4.1}_{-4.2}$  ppm, and  $65^{+15}_{-16}$  ppm, respectively. We also recovered this phase curve signal for the grazing hot Jupiter system HIP 65A, with a semiamplitude of  $30.4^{+8.5}_{-7.7}$  ppm.
- A marginal detection of a phase shift in the atmospheric brightness modulation signal was reported for WASP-100b, indicating an eastward offset in the region of maximum brightness on the dayside hemisphere of  $14.2 \pm 4.6$ . The results for this system are in broad agreement with those reported in the independent analysis by Jansen & Kipping (2020).
- HIP 65A, TOI-503, and WASP-30 display photometric variability associated with ellipsoidal distortion of the host star, with semiamplitudes of  $29.0^{+7.7}_{-7.9}$  ppm,  $60.2^{+7.4}_{-7.8}$  ppm, and  $101^{+22}_{-21}$  ppm, respectively. Only TOI-503 shows a robust Doppler boosting signal ( $30.1^{+7.4}_{-8.5}$  ppm) as well. The amplitudes of these measured signals are generally consistent with the predictions of theoretical models of the corresponding physical processes.
- We combined the measured *TESS* secondary eclipse depths for all systems with available *Spitzer*

3.6 and 4.5  $\mu\text{m}$  secondary eclipse data to simultaneously constrain the dayside brightness temperature and optical geometric albedo (Table 3). Of the targets discussed in this work, only WASP-100b ( $A_g = 0.26 \pm 0.07$ ) and WASP-121b ( $A_g = 0.27 \pm 0.04$ ; phase curve analyzed in Daylan et al. 2019) show enhanced geometric albedos.

- Using the geometric albedos measured in this paper and previous analyses of *TESS* phase curves, we found a tentative positive correlation between dayside temperature and optical geometric albedo, which suggests that planets with  $T_{\text{day}} > 2000$  K may have systematically higher atmospheric reflectivity due to high-temperature condensates and/or opacity sources contributing additional heating across the dayside atmosphere.

This work is the first systematic study of orbital phase curves provided by the *TESS* mission. These efforts will be expanded in the coming year with an analogous analysis of targets observed by *TESS* in the northern ecliptic hemisphere. Looking past the Primary Mission, all of the Sectors from the first two years of the *TESS* mission will be revisited during the approved Extended Mission, along with much of the Ecliptic to achieve almost full sky coverage, with possible further extensions in the future.

The availability of additional photometry will greatly refine existing phase curve fits, as well as recover statistically significant secondary eclipses and phase curve signals for many of the currently marginal cases. By narrowing the constraints on the amplitude and phase shift of the atmospheric brightness modulation, we will be able to carry out more detailed characterization of the temperature distribution and probe the possibility of inhomogeneous clouds, as have been detected on

Kepler-7b, for example (Demory et al. 2013; Shporer & Hu 2015). Simultaneously, the long time baseline spanned by these repeated observations will enable numerous other scientific objectives of interest, such as the search for orbital decay in short-period hot Jupiter systems (e.g., Yee et al. 2020) or the detection of temporal variability in exoplanet atmospheres (i.e., weather), which has been predicted by some recent modeling work (e.g., Komacek & Showman 2020).

The tentative trends in the visible-light geometric albedo values reported in Section 5.3 provide particularly fertile ground for follow-up study. With the end of the *Spitzer* era, we can look to near-future facilities such as *JWST* to continue space-based infrared observations, which, when combined with *TESS*-band secondary eclipses, will expand the set of direct albedo measurements and better probe the emergent trends. This, alongside other intensive atmospheric characterization campaigns, will yield new insights into the formation and properties of exoplanet clouds.

Funding for the *TESS* mission is provided by NASA's Science Mission directorate. This paper includes data collected by the *TESS* mission, which are publicly available from the Mikulski Archive for Space Telescopes (MAST). Resources supporting this work were provided by the NASA High-End Computing (HEC) Program through the NASA Advanced Supercomputing (NAS) Division at Ames Research Center for the production of the SPOC data products. We acknowledge Peter Gao, Tiffany Jansen, and David Kipping for helpful discussions that helped improve the manuscript. I.W. is supported by a Heising-Simons *51 Pegasi b* postdoctoral fellowship. T.D. acknowledges support from MIT's Kavli Institute as a Kavli postdoctoral fellow.

## REFERENCES

- Ackerman, A. S., & Marley, M. S. 2001, *ApJ*, 556, 872
- Addison, B. C., Wang, S., Johnson, M. C., et al. 2018, *AJ*, 156, 197
- Anderson, D. R., Brown, D. J. A., Collier Cameron, A., et al. 2014, *MNRAS*, submitted (arXiv:1410.3449)
- Anderson, D. R., Collier Cameron, A., Gillon, M., et al. 2012, *MNRAS*, 422, 1988
- Anderson, D. R., Collier Cameron, A., Hellier, C., et al. 2011, *ApJL*, 726, L19
- Anderson, D. R., Gillon, M., Hellier, C., et al. 2008, *MNRAS*, 387, L4
- Angerhausen, D., DeLarme, E., & Morse, J. A. 2015, *PASP*, 127, 1113
- Arcangeli, J., Désert, J.-M., Line, M. R., et al. 2018, *ApJL*, 855, L30
- Barclay, T., Huber, D., Rowe, J. F., et al. 2012, *ApJ*, 761, 53
- Bell, T. J., Nikolov, N., Cowan, N. B., et al. 2017, *ApJL*, 847, L2
- Benneke, B., Knutson, H. A., Lothringer, J., et al. 2019, *NatAs*, 3, 813
- Bento, J., Schmidt, B., Hartman, J. D., et al. 2017, *MNRAS*, 468, 835
- Bloemen, S., Marsh, T. R., Degroote, P., et al. 2012, *MNRAS*, 422, 2600
- Bourrier, V., Kitzmann, D., Kuntzer, T., et al. 2019, *A&A*, in revision (arXiv:1909.03010)
- Burkert, J., Quataert, E., Arras, P., & Weinberg, N. N. 2012, *MNRAS*, 421, 983
- Carmichael, T. W., Latham, D. W., & Vanderburg, A. M. 2019, *AJ*, 158, 38
- Claret, A. 2017, *A&A*, 600, A30
- Claret, A. 2018, *A&A*, 618, A20
- Cooper, C., Sudarsky, D., Milsom, J., Lunine, J., & Burrows, A. 2003, *ApJ*, 586, 1320
- Cowan, N. B., & Agol, E. 2011, *ApJ*, 729, 54
- Daylan, T., Günther, M. N., Mikal-Evans, T., et al. 2019, *AJ*, in revision (arXiv:1909.03000)
- Demory, B.-O., de Wit, J., Lewis, N., et al. 2013, *ApJL*, 776, L25
- Ehrenreich, D., Lagrange, A.-M., Bouchy, F., et al. 2011, *A&A*, 525, A85
- Enoch, B., Collier Cameron, A., & Horne, K. 2012, *A&A*, 540, A99
- Espinoza, N., Rackham, B. V., Jordán, A., et al. 2019, *MNRAS*, 482, 2065

- Esteves, L. J., De Mooij, E. J. W., & Jayawardhana, R. 2013, *ApJ*, 772, 51
- Esteves, L. J., De Mooij, E. J. W., & Jayawardhana, R. 2015, *ApJ*, 804, 150
- Evans, T. M., Pont, F., Sing, D. K., et al. 2013, *ApJL*, 772, L16
- Foreman-Mackey, D., Hogg, D. W., Lang, D., & Goodman, J. 2013, *PASP*, 125, 306
- Garhart, E., Deming, D., Mandell, A., et al. 2019, *AJ*, accepted (arXiv:1901.07040)
- Gelman, A., & Rubin, D. B. 1992, *StaSc*, 7, 457
- Gillon, M., Anderson, D. R., Collier-Cameron, A., et al. 2013, *A&A*, 552, A82
- Hellier, C., Anderson, D. R., Bouchy, F., et al. 2019, *MNRAS*, 482, 1379
- Hellier, C., Anderson, D. R., Cameron, A. C., et al. 2014, *MNRAS*, 440, 1982
- Hellier, C., Anderson, D. R., Collier Cameron, A., et al. 2011, *A&A*, 535, L7
- Hellier, C., Anderson, D. R., Collier Cameron, A., et al. 2017, *MNRAS*, 465, 3693
- Helling, Ch. 2019, *AREPS*, 47, 583
- Heng, K., & Demory, B.-O. 2013, *ApJ*, 777, 100
- Husser, T.-O., Wende-von Berg, S., Dreizler, S., et al. 2013, *A&A*, 553, A6
- Jansen, T., & Kipping, D. 2020, *MNRAS*, submitted (arXiv:2001.10580)
- Jenkins, J. M., Caldwell, D. A., Chandrasekaran, H., et al. 2010, *ApJL*, 713, L87
- Jenkins, J. M., & Doyle, L. R. 2003, *ApJ*, 595, 429
- Jenkins, J. M., Twicken, J. D., McCaulliff, S., et al. 2016, *Proc. SPIE*, 9913, 99133E
- Keating, D., & Cowan, N. B. 2017, *ApJL*, 849, L5
- Komacek, T. D., & Showman, A. P. 2020, *ApJ*, 888, 2
- Kreidberg, L. 2015, *PASP*, 127, 1161
- Laughlin, G., Crismani, M., & Adams, F. C. 2011, *ApJL*, 729, L7
- Loeb, A., & Gaudi, B. S. 2003, *ApJL*, 588, L117
- Lothringer, J., Barman, T., & Koskinen, T. 2018, *ApJ*, 866, 27
- Mallonn, M., Köhler, J., Alexoudi, X., et al. 2019, *A&A*, 624, A62
- Mansfield, M., Bean, J. P., Stevenson, K. B., et al. 2019, *ApJL*, 888, L15
- Marley, M. S., Ackerman, A. S., Cuzzi, J. N., & Kitzmann, D. 2013, in *Comparative Climatology of Terrestrial Planets*, ed. S. J. Mackwell, A. A. Simon-Miller, J. W. Harder, & M. A., Bullock (Tucson, AZ: University of Arizona Press), 367
- Marley, M. S., Saumon, D., Cushing, M., et al. 2013, *ApJ*, 754, 135
- Maxted, P. F. L., Anderson, D. R., Collier Cameron, A., et al. 2013, *PASP*, 125, 48
- Mayorga, L. C., Batalha, N. E., Lewis, N. K., & Marley, M. S. 2019, *AJ*, 158, 66
- Mazeh, T. 2008, *EAS Publications Series*, 29, 1
- Mireles, I., Shporer, A., Zhou, G., et al. 2020, *AJ*, in preparation
- Morris, S. L. 1985, *ApJ*, 295, 143
- Morris, S. L., & Naftilan, S. A. 1993, *ApJ*, 419, 344
- Nielsen, L. D., Brahm, R., Bouchy, F., et al. 2020, *A&A*, submitted (arXiv:2003.05932)
- Parmentier, V., & Crossfield, I. J. M. 2017, in *Handbook of Exoplanets*, ed. H. J. Deeg & J. A. Belmonte (Cham: Springer), 116
- Parmentier, V., Fortney, J. J., Showman, A. P., Morley, C., & Marley, M. S., 2016, *ApJ*, 828, 22
- Parmentier, V., Line, M. R., Bean, J. L., et al. 2018, *A&A*, 617, A110
- Perez-Becker, D., & Showman, A. P. 2013, *ApJ*, 776, 134
- Perna, R., Heng, K., & Pont, F. 2012, *ApJ*, 751, 59
- Pfahl, E., Arras, P., & Paxton, B. 2008, *ApJ*, 679, 783
- Powell, D., Loudon, T., Kreidberg, L., et al. 2019, *ApJ*, 887, 170
- Rodriguez, J. E., Colón, K. D., Stassun, K. G., et al. 2016, *ApJ*, 151, 138
- Rowe, J. F., Matthews, J. M., Seager, S., et al. 2008, *ApJ*, 689, 1345
- Shakura, N. I., & Postnov, K. A. 1987, *A&A*, 183, L21
- Shporer, A. 2017, *PASP*, 129, 072001
- Shporer, A., & Hu, R. 2015, *AJ*, 150, 112
- Shporer, A., Wong, I., Huang, C. X., et al. 2019, *AJ*, 157, 178
- Sing, D. K., Fortney, J. J., Nikolov, N., et al. 2016, *Natur*, 529, 59
- Smalley, B., Anderson, D. R., Collier-Cameron, A., et al. 2012, *A&A*, 547, A61
- Smith, A. M. S. 2015, *AcA*, 65, 117
- Smith, A. M. S., Anderson, D. R., Collier Cameron, A., et al. 2012, *AJ*, 143, 81
- Smith, J. C., Stumpe, M. C., Van Cleve, J. E., et al. 2012, *PASP*, 124, 1000
- Stassun, K. G., Collins, K. A., & Gaudi, B. S. 2017, *AJ*, 153, 136
- Stassun, K. G., Oelkers, R. J., Pepper, J., et al. 2018, *AJ*, 156, 102
- Stevenson, K. B., Line, M. R., Bean, J. L., et al. 2017, *AJ*, 153, 68
- Stumpe, M. C., Smith, J. C., Catanzarite, J. H., et al. 2014, *PASP*, 126, 100
- Šubjak, J., Sharma, R., Carmichael, T. W., et al. 2019, *AJ*, accepted (arXiv:1909.07984)
- Sullivan, P. W., Winn, J. N., Berta-Thompson, Z. K., et al. 2015, *ApJ*, 809, 77
- Triaud, A. H. M. J., Hebb, L., Anderson, D. R., et al. 2013, *A&A*, 549, A18
- Turner, O. D., Anderson, D. R., Collier Cameron, A., et al. 2016, *PASP*, 128, 064401
- van Kerkwijk, M. H., Rappaport, S. A., Breton, R. P., et al. 2010, *ApJ*, 715, 51
- West, R. G., Hellier, C., Almenara, J.-M., et al. 2016, *A&A*, 585, A126
- Wilson, D. M., Gillon, M., Hellier, C., et al. 2008, *ApJL*, 675, L113
- Wong, I., Benneke, B., Gao, P., et al. 2020a, *ApJ*, in revision
- Wong, I., Benneke, B., Shporer, A., et al. 2020b, *AJ*, 159, 104
- Wong, I., Shporer, A., Becker, J. C., et al. 2020c, *AJ*, 159, 29
- Wong, I., Shporer, A., Morris, B. M., et al. 2020d, *AJ*, in revision (arXiv:1910.01607)
- Yee, S. W., Winn, J. N., Knutson, H. A., et al. 2020, *ApJL*, 888, L5
- Zucker, S., Mazeh, T., & Alexander, T. 2007, *ApJ*, 670, 1326

## APPENDIX

The table below lists all of the data segments extracted from the *TESS* light curves for the 19 systems analyzed in this paper. In the second column, each segment is referred to by a three number sequence separated by dashes: the first number denotes the *TESS* Sector, the second number indicates the spacecraft orbit (two per Sector), and the last digit is a sequential data segment number. Only data segments with time series spanning longer than 1 day are included in the table and were considered in our analysis; for example, during *TESS* Sectors 1 and 2, a momentum dump was scheduled within the last day of observation during each spacecraft orbit, and we discarded the short segment of photometry between the final momentum dump and the break in data collection for downlink. The number of data points before and after flagged data removal, outlier trimming, and ramp trimming are indicated, as well as the start and final time stamps of each data segment. The sixth column lists the order of the polynomial detrending function used for the respective segment (see Section 2). The final column indicates whenever data was removed to alleviate flux ramps and other uncorrectable systematic artifacts. Several of the segments showed severe short-term (i.e., on timescales comparable to or shorter than the orbital period) photometric variations due to uncorrected instrumental systematics. These are also indicated under the Comments column and were removed from the light curve prior to our joint fits.

**Table 4.** Summary of Light Curve Segments

Target	Segment <sup>a</sup>	$n_{\text{raw}}$ <sup>b</sup>	$n_{\text{trimmed}}$ <sup>b</sup>	$T_{\text{start}}$ <sup>c</sup>	$T_{\text{end}}$ <sup>c</sup>	Order <sup>d</sup>	Comments
HATS-24	13-1-1	2470	2413	653.925	657.339	3	
	13-1-2	2430	2339	657.350	660.714	2	
	13-1-3	2430	2380	660.725	664.089	3	
	13-1-4	2589	2491	664.100	667.695	3	
	13-2-1	2473	2412	668.631	672.047	2	
	13-2-2	2430	2357	672.058	675.422	4	
	13-2-3	2430	2390	675.433	678.797	2	
	13-2-4	2430	2385	678.808	682.172	0	
HIP 65A	1-1-1	1839	1774	325.299	327.838	4	
	1-1-2	1800	1390	327.855	329.841	1	trimmed 0.50 d from end
	1-1-3	1800	1706	330.355	332.831	3	
	1-1-4	1800	1727	332.855	335.330	4	
	1-1-5	1800	1730	335.354	337.834	2	
	1-2-1	1828	1774	339.665	342.183	2	
	1-2-2	1800	1749	342.197	344.683	3	
	1-2-3	1800	1761	344.697	347.183	3	
	1-2-4	1800	875	347.445	349.683	3	trimmed 0.25 d from start
	1-2-5	1800	1748	349.697	352.183	2	
	2-1-1	1827	1778	354.113	356.632	3	
	2-1-2	1800	1741	356.651	359.132	3	
	2-1-3	1800	1742	359.151	361.631	3	
	2-1-4	1800	1739	361.651	364.131	3	
	2-1-5	1800	1736	364.151	366.631	3	
	2-2-1	1827	1766	368.606	371.124	3	
	2-2-2	1800	1750	371.144	373.624	3	
	2-2-3	1800	1741	373.644	376.124	2	
	2-2-4	1800	1713	376.144	378.602	3	
	2-2-5	1800	1718	378.644	381.124	2	
TOI-503	7-1-1	2288	2070	491.887	494.798	0	trimmed 0.25 d from start
	7-1-2	2250	2207	494.810	497.923	1	
	7-1-3	2250	2223	497.935	501.049	2	
	7-1-4	1429	1403	501.060	503.043	0	
	7-2-1	2280	2066	504.961	507.861	0	trimmed 0.25 d from start
	7-2-2	2250	2207	507.872	510.986	0	
	7-2-3	2250	2039	510.997	514.111	0	trimmed 511.75—512.00
	7-2-4	1419	1394	514.122	516.092	0	

*Table 4 continued*

**Table 4** (*continued*)

Target	Segment <sup>a</sup>	$n_{\text{raw}}$ <sup>b</sup>	$n_{\text{trimmed}}$ <sup>b</sup>	$T_{\text{start}}$ <sup>c</sup>	$T_{\text{end}}$ <sup>c</sup>	Order <sup>d</sup>	Comments
WASP-4	2-1-1	1827	1768	354.114	356.632	2	
	2-1-2	1800	1743	356.652	359.132	0	
	2-1-3	1800	1726	359.152	361.632	1	
	2-1-4	1800	1747	361.652	364.132	0	
	2-1-5	1800	1399	364.152	366.132	0	trimmed 0.50 d from end
	2-2-1	1827	1593	368.859	371.125	2	trimmed 0.25 d from start
	2-2-2	1800	1758	371.145	373.625	1	
	2-2-3	1800	1739	373.645	376.125	1	
	2-2-4	1800	1714	376.145	378.603	0	
	2-2-5	1800	1725	378.645	381.125	2	
WASP-5	2-1-1	1827	1760	354.114	356.632	2	
	2-1-2	1800	1747	356.652	359.132	1	
	2-1-3	1800	1736	359.152	361.632	3	
	2-1-4	1800	1742	361.652	364.132	0	
	2-1-5	1800	1735	364.152	366.632	0	
	2-2-1	1827	1775	368.607	371.125	0	
	2-2-2	1800	1743	371.145	373.625	0	
	2-2-3	1800	1732	373.645	376.125	2	
	2-2-4	1800	1715	376.145	378.603	1	
	2-2-5	1800	1718	378.645	381.125	1	
WASP-30	2-1-1	1827	1761	354.115	356.633	0	
	2-1-2	1800	1394	356.652	359.133	0	trimmed 358.1—358.6
	2-1-3	1800	1743	359.153	361.633	0	
	2-1-4	1800	1732	361.653	364.133	1	
	2-1-5	1800	1742	364.153	366.633	0	
	2-2-1	1827	1783	368.608	371.126	0	
	2-2-2	1800	1742	371.146	373.626	0	
	2-2-3	1800	1750	373.646	376.126	0	
	2-2-4	1800	1711	376.146	378.604	0	
	2-2-5	1800	1728	378.646	381.126	1	
WASP-36	8-1-1	2283	1851	517.902	520.506	0	trimmed 0.50 d from start
	8-1-2	2250	2205	520.518	523.631	1	
	8-1-3	2250	2214	523.643	526.756	0	
	8-1-4	1659	1637	526.768	529.070	0	
	8-2-1	1121	...	535.009	536.548	...	severe systematics
	8-2-2	2250	2214	536.559	539.673	2	
	8-2-3	1672	1645	539.684	542.005	2	
WASP-43	9-1-1	1548	1371	544.441	546.382	3	
	9-1-2	2250	2213	546.393	549.507	2	
	9-1-3	2250	2218	549.518	552.632	4	
	9-1-4	2092	2057	552.643	555.547	2	
	9-2-1	1627	912	558.105	559.902	2	trimmed 0.25 d from start
	9-2-2	2250	2207	559.913	563.027	5	
	9-2-3	2250	2219	563.038	566.152	1	
	9-2-4	1669	1640	566.163	568.480	2	
WASP-46	1-1-1	1839	1766	325.300	327.839	0	
	1-1-2	1800	1685	327.856	330.328	2	
	1-1-3	1800	1692	330.356	332.832	3	
	1-1-4	1800	1723	332.856	335.331	1	
	1-1-5	1800	1738	335.354	337.835	0	
	1-2-1	1828	1770	339.665	342.183	2	
	1-2-2	1800	1746	342.197	344.683	2	
	1-2-3	1800	1753	344.697	347.183	0	
	1-2-4	1800	1038	347.197	349.683	0	

*Table 4 continued*

**Table 4** (*continued*)

Target	Segment <sup>a</sup>	$n_{\text{raw}}$ <sup>b</sup>	$n_{\text{trimmed}}$ <sup>b</sup>	$T_{\text{start}}$ <sup>c</sup>	$T_{\text{end}}$ <sup>c</sup>	Order <sup>d</sup>	Comments
WASP-64	1-2-5	1800	1755	349.697	352.183	0	
	6-1-1	2250	2211	468.390	471.504	2	
	6-1-2	2250	2200	471.515	474.629	1	
	6-1-3	1717	1691	474.640	477.024	2	
	6-2-1	2288	2058	478.370	481.275	0	trimmed 0.25 d from start
	6-2-2	2250	2206	481.286	484.400	0	
	6-2-3	2250	2216	484.411	487.525	2	
	6-2-4	1809	1780	487.536	490.048	2	
	7-1-1	2288	2248	491.635	494.796	0	
	7-1-2	2250	2203	494.807	497.921	1	
	7-1-3	2250	2218	497.932	501.046	0	
	7-1-4	1429	1411	501.057	503.041	1	
	7-2-1	2280	2232	504.709	507.858	2	
	7-2-2	2250	2217	507.870	510.983	0	
	7-2-3	2250	2204	510.996	514.108	1	
	7-2-4	1419	1401	514.119	516.089	1	
WASP-72	3-1-1	1405	1270	385.952	387.750	0	
	3-1-2	1800	1738	387.769	390.250	0	
	3-1-3	1800	1726	390.269	392.750	0	
	3-1-4	1800	1736	392.769	395.250	0	
	3-2-1	1585	1277	396.889	398.710	0	trimmed 0.25 d from start
	3-2-2	1440	1386	398.729	400.710	0	
	3-2-3	1440	1393	400.729	402.710	2	
	3-2-4	1440	1388	402.729	404.710	2	
	3-2-5	1221	1045	404.729	406.218	0	
	4-1-1	2191	1604	410.907	413.189	0	trimmed 0.75 d from the end
	4-1-2	2160	2123	413.958	416.939	1	
	4-1-3	1110	1060	416.958	418.492	0	
	4-1-4	1249	1219	421.218	422.939	0	
	4-2-1	2186	2136	424.560	427.584	1	
	4-2-2	2160	2117	427.604	430.584	2	
	4-2-3	2160	2117	430.604	433.584	2	
	4-2-4	2160	2120	433.604	436.584	2	
WASP-77A	4-1-1	2191	2119	410.908	413.940	2	
	4-1-2	2160	2107	413.959	416.940	3	
	4-1-3	1110	...	416.959	418.493	...	severe systematics
	4-1-4	1249	...	421.219	422.940	...	severe systematics
	4-2-1	2190	2134	424.561	427.586	4	
	4-2-2	2160	2107	427.605	430.586	3	
	4-2-3	2160	2109	430.605	433.586	2	
	4-2-4	2160	2108	433.605	436.586	3	
WASP-78	5-1-1	2200	2155	437.996	441.026	2	
	5-1-2	2160	2126	441.037	444.026	1	
	5-1-3	2160	2130	444.037	447.026	0	
	5-1-4	2160	2130	447.037	450.026	0	
	5-2-1	2193	2159	451.560	454.589	0	
	5-2-2	2160	2117	454.600	457.589	0	
	5-2-3	2160	2135	457.600	460.589	1	
	5-2-4	2160	2117	460.600	463.589	1	
WASP-82	5-1-1	2200	2161	437.997	441.027	0	
	5-1-2	2160	1945	441.038	443.779	1	trimmed 0.25 d from end
	5-1-3	2160	1943	444.287	447.027	1	trimmed 0.25 d from start
	5-1-4	2160	2116	447.039	450.027	1	
	5-2-1	2193	1802	451.561	454.091	1	trimmed 0.50 d from end

*Table 4 continued*

**Table 4** (*continued*)

Target	Segment <sup>a</sup>	$n_{\text{raw}}$ <sup>b</sup>	$n_{\text{trimmed}}$ <sup>b</sup>	$T_{\text{start}}$ <sup>c</sup>	$T_{\text{end}}$ <sup>c</sup>	Order <sup>d</sup>	Comments
	5-2-2	2160	...	454.601	457.590	...	severe systematics
	5-2-3	2160	...	457.601	460.590	...	severe systematics
	5-2-4	2160	1948	460.601	463.340	2	trimmed 0.25 d from end
WASP-100	1-1-1	1839	1418	325.796	327.835	0	trimmed 0.50 d from start
	1-1-2	1800	1692	327.852	330.324	0	
	1-1-3	1800	1707	330.352	332.828	0	
	1-1-4	1800	1729	332.852	335.327	0	
	1-1-5	1800	1737	335.350	337.831	0	
	1-2-1	1828	1417	340.162	342.180	0	trimmed 0.50 d from start
	1-2-2	1800	1392	342.692	344.680	1	trimmed 0.50 d from start
	1-2-3	1800	1771	344.694	347.180	0	
	1-2-4	1800	1033	347.194	349.680	0	
	1-2-5	1800	1736	349.694	352.180	0	
	2-1-1	1827	1776	354.110	356.628	1	
	2-1-2	1800	1751	356.648	359.128	0	
	2-1-3	1800	1736	359.148	361.628	0	
	2-1-4	1800	1748	361.648	364.129	0	
	2-1-5	1800	1746	364.148	366.629	2	
	2-2-1	1827	1774	368.604	371.122	0	
	2-2-2	1800	1750	371.141	373.622	0	
	2-2-3	1800	1749	373.641	376.122	1	
	2-2-4	1800	1713	376.141	378.599	1	
	2-2-5	1800	1725	378.641	381.122	1	
	3-1-1	1405	1272	385.949	387.747	0	
	3-1-2	1800	1736	387.766	390.247	0	
	3-1-3	1800	1739	390.266	392.747	1	
	3-1-4	1800	1724	392.766	395.247	2	
	3-2-1	1586	1459	396.636	398.706	0	
	3-2-2	1440	1385	398.726	400.706	1	
	3-2-3	1440	1399	400.726	402.706	0	
	3-2-4	1440	1044	402.726	404.206	0	trimmed 0.50 d from end
	3-2-5	1222	1049	404.726	406.215	0	
	4-1-1	2191	2111	410.904	413.935	1	
	4-1-2	2160	2115	413.955	416.935	0	
	4-1-3	1110	1080	416.955	418.488	0	
	4-2-1	2186	2136	424.556	427.581	1	
	4-2-2	2160	2113	427.601	430.581	1	
	4-2-3	2160	2117	430.601	433.581	0	
	4-2-4	2160	1757	433.601	436.081	1	trimmed 0.50 d from end
	5-1-1	2200	1792	438.494	441.023	0	trimmed 0.50 d from start
	5-1-2	2160	2116	441.034	444.023	0	
	5-1-3	2160	2110	444.034	447.023	0	
	5-1-4	2160	2123	447.034	450.023	0	
	5-2-1	2193	1798	452.057	454.585	2	trimmed 0.50 d from start
	5-2-2	2160	2115	454.596	457.585	0	
	5-2-3	2160	2130	457.596	460.585	1	
	5-2-4	2160	2118	460.596	463.585	0	
	6-1-1	2250	...	468.388	471.501	...	severe systematics
	6-1-2	2250	...	471.513	474.626	...	severe systematics
	6-1-3	1717	...	474.637	477.021	...	severe systematics
	6-2-1	2288	1344	479.371	481.272	2	trimmed 1.25 d from start
	6-2-2	2250	2210	481.283	484.397	0	
	6-2-3	2250	2211	484.408	487.522	2	
	6-2-4	1809	1790	487.533	490.044	0	

*Table 4 continued*

Table 4 (continued)

Target	Segment <sup>a</sup>	$n_{\text{raw}}$ <sup>b</sup>	$n_{\text{trimmed}}$ <sup>b</sup>	$T_{\text{start}}$ <sup>c</sup>	$T_{\text{end}}$ <sup>c</sup>	Order <sup>d</sup>	Comments
	7-1-1	2288	1892	492.133	494.793	0	trimmed 0.50 d from start
	7-1-2	2250	2209	494.804	497.918	0	
	7-1-3	2250	2203	497.929	501.043	0	
	7-1-4	1429	1407	501.054	503.037	1	
	7-2-1	2280	1876	505.211	507.855	0	trimmed 0.50 d from start
	7-2-2	2250	2212	507.866	510.980	1	
	7-2-3	2250	2207	510.991	514.105	0	
	7-2-4	1419	1400	514.116	516.085	0	
	8-1-1	2283	2190	517.397	520.501	1	
	8-1-2	2250	2200	520.512	523.626	0	
	8-1-3	2250	2201	523.637	526.751	1	
	8-1-4	1659	1630	526.762	529.064	2	
	8-2-1	1121	...	535.003	536.542	...	severe systematics
	8-2-2	2250	2207	536.553	539.667	2	
	8-2-3	1672	1649	539.678	541.999	1	
	9-1-1	1227	885	545.134	546.375	1	trimmed 0.25 d from start
	9-1-2	2250	2215	546.387	549.500	3	
	9-1-3	2250	2225	549.511	552.624	0	
	9-1-4	2092	2054	552.636	555.541	2	
	9-2-1	1313	...	558.284	559.896	...	sever systematics
	9-2-2	2250	2205	559.907	563.021	0	
	9-2-3	2250	2212	563.032	566.146	2	
	9-2-4	1669	1638	566.157	568.474	2	
	10-1-1	1623	1454	570.560	572.604	1	
	10-1-2	2250	1678	573.364	575.729	2	trimmed 0.75 d from start
	10-1-3	2250	2211	575.741	578.854	1	
	10-1-4	2102	2070	578.866	581.784	2	
	10-2-1	1324	986	584.538	585.917	0	trimmed 0.25 d from start
	10-2-2	2250	2211	585.928	589.042	0	
	10-2-3	2250	1681	589.802	592.167	0	trimmed 0.75 d from start
	10-2-4	2522	2126	592.677	595.680	2	trimmed 0.50 d from start
	11-1-1	2250	2161	599.952	603.063	1	
	11-1-2	2250	2190	603.074	606.188	0	
	11-1-3	2517	2476	606.199	609.694	2	
	11-2-1	1044	...	612.698	613.938	...	severe systematics
	11-2-2	2250	2030	614.199	617.063	0	trimmed 0.25 d from start
	11-2-3	2250	2035	617.323	620.188	1	trimmed 0.25 d from start
	11-2-4	2659	2624	620.199	623.891	3	
	12-1-1	2280	...	624.962	628.105	...	severe systematics
	12-1-2	2250	2141	628.119	631.230	0	
	12-1-3	2250	2184	631.244	634.355	2	
	12-1-4	2250	2189	634.366	637.480	1	
	12-1-5	1084	1010	637.491	638.995	1	
	12-2-1	2280	...	640.038	643.188	...	severe systematics
	12-2-2	2250	2203	643.199	646.313	0	
	12-2-3	2250	2209	646.325	649.438	1	
	12-2-4	2479	2438	649.450	652.891	2	
	13-1-1	2470	2414	653.920	657.334	2	
	13-1-2	2430	2337	657.346	660.709	2	
	13-1-3	2430	2375	660.721	664.085	2	
	13-1-4	2589	2494	664.096	667.690	2	
	13-2-1	2473	2405	668.626	672.043	2	
	13-2-2	2430	2360	672.054	675.418	1	
	13-2-3	2430	2389	675.429	678.793	1	

Table 4 continued

**Table 4** (*continued*)

Target	Segment <sup>a</sup>	$n_{\text{raw}}$ <sup>b</sup>	$n_{\text{trimmed}}$ <sup>b</sup>	$T_{\text{start}}$ <sup>c</sup>	$T_{\text{end}}$ <sup>c</sup>	Order <sup>d</sup>	Comments
WASP-111	13-2-4	2430	2389	678.806	682.168	2	
	1-1-1	1839	1765	325.301	327.840	2	
	1-1-2	1800	1699	327.857	330.329	0	
	1-1-3	1800	1699	330.357	332.833	1	
	1-1-4	1800	1731	332.857	335.332	1	
	1-1-5	1800	1742	335.356	337.836	0	
	1-2-1	1828	1762	339.667	342.185	2	
	1-2-2	1800	1743	342.199	344.685	2	
	1-2-3	1800	1758	344.699	347.185	3	
WASP-122/KELT-14	1-2-4	1800	1029	347.199	349.685	0	
	1-2-5	1800	1742	349.699	352.185	1	
	7-1-1	2288	2234	491.634	494.795	2	
	7-1-2	2250	2211	494.806	497.920	0	
	7-1-3	2250	2208	497.932	501.045	1	
	7-1-4	1429	1403	501.057	503.040	0	
	7-2-1	2280	1890	505.208	507.858	2	trimmed 0.50 d from start
	7-2-2	2250	2215	507.869	510.983	3	
	7-2-3	2250	2222	510.994	514.108	0	
WASP-142	7-2-4	1419	1399	514.119	516.088	0	
	8-1-1	2283	1851	517.901	520.506	2	trimmed 0.50 d from start
	8-1-2	2250	2215	520.518	523.631	0	
	8-1-3	2250	2222	523.642	526.756	1	
	8-1-4	1659	1632	526.767	529.070	0	
	8-2-1	1121	...	535.009	536.547	...	severe systematics
	8-2-2	2250	2202	536.559	539.672	0	
	8-2-3	1672	1653	539.684	542.004	1	
WASP-173A	2-1-1	1827	1773	354.115	356.633	4	
	2-1-2	1800	1742	356.652	359.133	3	
	2-1-3	1800	1736	359.152	361.631	4	
	2-1-4	1800	1755	361.652	364.133	3	
	2-1-5	1800	1749	364.152	366.633	3	
	2-2-1	1827	1771	368.608	371.126	3	
	2-2-2	1800	1750	371.145	373.626	2	
	2-2-3	1800	1744	373.645	376.126	3	
	2-2-4	1800	1713	376.145	378.603	3	
	2-2-5	1800	1733	378.645	381.126	4	

**Notes.**

<sup>a</sup> The numbers indicate the *TESS* Sector, spacecraft orbit (two per Sector), and segment number, respectively.

<sup>b</sup> Number of data points contained in each data segment before and after removing flagged points, filtering out outliers, and trimming ramps (as detailed under Comments).

<sup>c</sup> Start and end times of each data segment, in units of  $\text{BJD}_{\text{TDB}} - 2458000$ .

<sup>d</sup> Order of the polynomial systematics detrending model used in the final joint fits.